

## Diplomarbeit

# Pilot-Symbol-Aided OFDM Channel Estimation in Doubly-Selective Channels

ausgeführt zum Zwecke der Erlangung des akademischen Grades eines  
Diplom-Ingenieurs

unter der Leitung von

Univ.Prof. Dipl.-Ing. Dr.techn. Markus Rupp

Dipl.-Ing. Dr.techn. Michal Šimko

Dipl.-Ing. Martin Lerch

Institute of Telecommunications

eingereicht an der Technischen Universität Wien  
Fakultät für Elektrotechnik und Informationstechnik

von

**Ronald Nissel**

0551696

Rauchfangkehrergasse 4/14

1150 Wien

Wien, November 2013

---

I hereby certify that the work reported in this thesis is my own,  
and the work done by other authors is appropriately cited.

Ronald Nissel  
Vienna, November 22, 2013

---

# Abstract

Nowadays, most wireless communication standards utilize Orthogonal Frequency Division Multiplexing (OFDM) as their modulation technique. For coherent detection, the performance of such systems depends strongly on the accuracy of the channel estimation. One possible estimation technique is Pilot-symbol-Aided Channel Estimation (PACE), which allows the reconstruction of the channel by means of interpolation.

In this master thesis, I derive a closed-form expression for the Bit Error Probability (BEP) of an OFDM system that utilizes two-dimensional PACE. I assume Rayleigh fading, Gaussian noise and a linear, but other otherwise completely arbitrary, interpolation. For a Signal-to-Interference Ratio (SIR) larger than the signal-to-noise ratio, simulations confirm the analytical results. However, for a lower SIR they exhibit small differences because the Inter-Carrier Interference (ICI) is not Gaussian distributed, violating my assumption. Indeed, analytical calculation of the ICI probability density function (pdf) verifies that even for infinite many subcarriers, the pdf does not approach a Gaussian distribution.

It is further shown that the well-known Minimum Mean Squared Error (MMSE) estimation also minimizes the BEP and that, for certain assumptions, the optimal 2D interpolation can be performed in an equivalent way by successively 1D-1D interpolations of the MMSE pilot-symbol estimates. A numerical example then compares different interpolation methods (optimum, linear<sup>1</sup>, spline, and natural neighbor) in terms of BEP.

Finally, the analytical BEP is validated by real world measurements, utilizing the Vienna Wireless Testbed in combination with a Rotation Unit, allowing repeatable and controllable measurements at high velocities.

---

<sup>1</sup> in the sense of a straight line

---

# Kurzfassung

In den meisten Standards zur drahtlosen Kommunikation wird heutzutage Orthogonal Frequency Division Multiplexing (OFDM) als Modulationsverfahren verwendet. Für den Fall der kohärenten Detektion, hängt die Leistungsfähigkeit entscheidend von der Kanalschätzung (z.B.: Pilot-symbol-Aided Channel Estimation (PACE)) ab. Bei PACE wird der Kanal unter Zuhilfenahme von Interpolation rekonstruiert.

In dieser Diplomarbeit werde ich für ein OFDM System, welches PACE verwendet, einen analytischen Ausdruck für die Bitfehlerwahrscheinlichkeit (BEP) herleiten. Ich nehme hierzu Rayleigh Schwund, gaußsches Rauschen und eine lineare, sonst jedoch beliebige, Interpolation an. Falls das Signal-Inferenz-Verhältnis (SIR) größer als das Signal-Rausch-Verhältnis ist, bestätigen Simulationen die analytischen Berechnungen. Für ein niedrigeres SIR jedoch weisen Simulation und Berechnung kleine Unterschiede auf, da die Inter-Carrier Interference (ICI) nicht Gaußverteilt ist und damit meine Annahme verletzt. Eine Berechnung der Wahrscheinlichkeitsdichte der ICI bestätigt, dass diese nicht Gaußverteilt ist, selbst für unendlich viele Subcarrier

Es wird weiters gezeigt, dass die “Minimum Mean Squared Error” Schätzung ebenfalls die BEP minimiert und, dass, unter bestimmten Voraussetzungen, die optimale 2D Interpolation in äquivalenter Weise durch zwei 1D Interpolationen realisiert werden kann. Anhand eines numerischen Beispiels wird die BEP für verschiedene Interpolationsmethoden (Optimal, Linear<sup>2</sup>, Spline, natürliche Nachbarn) verglichen.

Zum Abschluss wird die Korrektheit der analytische BEP Gleichung durch Messungen verifiziert, wobei dafür das “Vienna Wireless Testbed” in Kombination mit einer Rotationseinheit verwendet wird. Dieses ermöglicht wiederholbare und kontrollierbare Messungen bei hohen Geschwindigkeiten.

---

<sup>2</sup> im Sinne einer geraden Linie

# Contents

<b>1</b>	<b>Introduction</b>	<b>1</b>
<b>2</b>	<b>System Model</b>	<b>4</b>
2.1	Doubly-Selective Channels . . . . .	4
2.2	Orthogonal Frequency Division Multiplexing . . . . .	7
<b>3</b>	<b>Inter-Carrier Interference</b>	<b>12</b>
3.1	Inter-Carrier Interference Power . . . . .	12
3.2	L-Dimensional Probability Density Function . . . . .	15
3.3	One-Dimensional Probability Density Function . . . . .	16
<b>4</b>	<b>Pilot-Symbol-Aided Channel Estimation</b>	<b>19</b>
4.1	Mean Squared Error . . . . .	21
4.2	Bit Error Probability . . . . .	23
4.2.1	4-QAM . . . . .	24
4.2.2	16-QAM . . . . .	27
4.2.3	Simulations . . . . .	30
4.3	Interpolation . . . . .	32
4.3.1	Optimal Interpolation . . . . .	34
4.3.2	Linear Interpolation . . . . .	36
4.3.3	Spline Interpolation . . . . .	37
4.3.4	Natural Neighbor Interpolation . . . . .	38
<b>5</b>	<b>Measurements</b>	<b>42</b>
5.1	Overview of the Measurement Set-Up . . . . .	42
5.2	Measurement Methodology . . . . .	44
5.3	Results . . . . .	48
<b>6</b>	<b>Conclusion and Outlook</b>	<b>51</b>
<b>A</b>	<b>OFDM Matrix of a vectorized Channel</b>	<b>53</b>

<b>B Correlation Matrices for a 2D separable WSSUS Channel</b>	<b>54</b>
<b>C BEP for 16-QAM</b>	<b>56</b>
<b>Acronyms</b>	<b>58</b>
<b>Bibliography</b>	<b>60</b>

# 1. Introduction

Orthogonal Frequency Division Multiplexing (OFDM) is the predominant modulation technique in today's wireless communication systems (e.g., Digital Video Broadcasting - Terrestrial (DVB-T), Wireless Local Area Network (WLAN), and Long Term Evolution (LTE)). The main advantages of OFDM are:

- the capability to deal with frequency-selective channels in an efficient way,
- the possibility to use simple equalizer, and
- a high spectral efficiency.

Although OFDM was already suggested in the 1960s[1], a widespread use has been possible only since the early 1990s because the required digital signal processors have become cheaper and more powerful.

For coherent OFDM detection, the channel has to be estimated. This becomes quite challenging for mobile wireless communication systems due to time-variant multipath propagation, which leads to doubly-selective channels, i.e., frequency-selective as well as time-selective, the latter causing Inter-Carrier Interference (ICI). Authors of [2–4] model ICI as Gaussian noise, claiming that the central limit theorem can be applied. This approximation is false, as already shown in [5] for phase noise and [6] for Nakagami-m channels and a linear channel variation. Based on the System model derived in Chapter 2, I calculate the probability density function (pdf) of the ICI and show that it does not approach a Gaussian distribution.

In this thesis, the channel estimation is performed by Pilot-symbol-Aided Channel Estimation (PACE). Here, in a first step, known symbols are used to estimate the channel at pilot positions. In a second step, the channel at data position is estimated by interpolation, such as:

- optimal interpolation: minimizes the Bit Error Probability (BEP)
- linear interpolation: straight line (plane) between two (three) points
- spline interpolation: piecewise cubic polynomials that satisfy certain smoothness conditions
- natural neighbor interpolation: based on the “stolen” area of a Voronoi diagram

Authors of [7–10] compared different interpolation methods (e.g., linear, spline, low-pass) in terms of Bit Error Ratio (BER). However, their comparison is only based on simulations, not offering analytical insights. This motivates the derivation of a closed-form expression for the BEP under PACE. Note that the derivation assumes a Rayleigh channel and Gaussian noise. As already mentioned above, the ICI is not Gaussian distributed, so that the calculated BEP represents only an approximation if the ICI power is higher than the noise power.

A theory is only useful if its prediction is supported by measurements in real world scenarios. I thus utilize the Vienna Wireless Testbed in order to compare the analytical BEP with the measured BER.

## Chapter Overview

**Chapter 2** describes the channel model and how it can be characterized by second order statistics. Furthermore, the principle of OFDM is explained and in particular, it is shown how to model an OFDM system by a matrix multiplication. In **Chapter 3**, the effect of ICI is investigated. Equations for the ICI-power as well as the ICI-pdf are provided. **Chapter 4** illustrates the concept of PACE and delivers a closed-form expression for the Mean Squared Error (MSE) and the BEP. It is shown that the Minimum Mean Squared Error (MMSE) estimation also minimizes the BEP<sup>1</sup>. The simulated BER is then compared to the analytical solution. Finally, the closed-form expression

---

<sup>1</sup> For 16-QAM, the MMSE estimation is only a close approximation of the optimal interpolation

of the BEP is used to compare different interpolation methods. **Chapter 5** describes how the real world measurement was performed and compares the measured BER with its theoretical prediction.

## 2. System Model

### 2.1. Doubly-Selective Channels

Mobile wireless communication channels are characterized by time-varying multipath propagation i.e. due to multiple scatterers, the electromagnetic signal can propagate along several different paths[11]. Suppose as a simplified example (time-invariant) that there are only two propagation path, attenuated by  $h_1$  and  $h_2$ , and delayed by  $\tau_1$  and  $\tau_2$ . Then, the received signal  $r(t)$  depends on the transmitted signal  $s(t)$  as follows:

$$r(t) = h_1 s(t - \tau_1) + h_2 s(t - \tau_2). \quad (2.1)$$

Taking the Fourier transform<sup>1</sup> leads to:

$$|R(f)| = |S(f)| \sqrt{h_1^2 + h_2^2 + 2h_1 h_2 \cos(2\pi(\tau_1 - \tau_2)f)}. \quad (2.2)$$

Equation (2.2) shows that different frequencies are attenuated differently, which is called frequency-selectivity ( $\tau_1 \neq \tau_2$ ). On the other hand, the effect of time variation always implies some sort of movement. Assuming only one path and a homogeneous plane wave, the received field strength  $E(t)$  can

---

<sup>1</sup>  $R(f) = \int_{-\infty}^{\infty} r(t) e^{-j2\pi f t} dt$

be written as [12]:

$$E(t) \propto \cos \left( 2\pi f_c t - \frac{2\pi}{\lambda}(d_0 + vt) \right), \quad (2.3)$$

whereas  $f_c$  denotes the carrier frequency,  $\lambda$  the wavelength,  $d_0$  the initial distance between transmitter and receiver and  $v$  the relative velocity. Equation (2.3) shows that the received signal is frequency-shifted by the Doppler shift:

$$\nu = -f_c \frac{v}{c_0}, \quad (2.4)$$

where  $c_0$  denotes the speed of light ( $2.998 \cdot 10^8$  m/s). I now assume a second path that has a different Doppler shift but equal delay<sup>2</sup>. The received signal can then be written as<sup>3</sup>:

$$R(f) = h_1 S(f - \nu_1) + h_2 S(f - \nu_2), \quad (2.5)$$

and, by taking the inverse Fourier transform

$$|r(t)| = |s(t)| \sqrt{h_1^2 + h_2^2 + 2h_1 h_2 \cos(2\pi(\nu_1 - \nu_2)t)}, \quad (2.6)$$

Equation (2.6) shows that different time positions are attenuated differently, which is called time-selectivity.

Equation (2.2) and (2.6) are closely related: Multipath propagation causes frequency-selectivity if the delays  $\tau_m$  are different and time-selectivity if the Doppler shifts  $\nu_m$  are different. If both of these effects apply at the same time, the channel is called doubly-selective.

According to the considerations above, a Linear Time Variant (LTV) channel can be characterized by a time-variant impulse response  $h(t, \tau)$ :

$$h(t, \tau) = \sum_{m=1}^M h_m e^{j(2\pi\nu_m t)} \delta(\tau - \tau_m), \quad (2.7)$$

or, in an equivalent way, by a time-variant transfer function  $H(t, f)$ :

$$H(t, f) = \int_{-\infty}^{\infty} h(t, \tau) e^{-j2\pi f \tau} d\tau. \quad (2.8)$$

---

<sup>2</sup> is set to zero

<sup>3</sup> signal bandwidth  $\ll f_c$

In reality, however, a complete deterministic characterization of  $h(t, \tau)$  is not feasible, which motivates the use of a stochastic description (second-order). These autocorrelation functions generally depend on four variables but by assuming Wide-Sense Stationary Uncorrelated Scattering (WSSUS) [13], the number of variables reduces to two so that the time-frequency correlation function becomes:

$$\mathbb{E} \{H(t, f)H^*(t', f')\} = R_H(t - t', f - f'). \quad (2.9)$$

Such a WSSUS channel can be modeled as [14]:

$$H(t, f) = \lim_{M \rightarrow \infty} \frac{1}{\sqrt{M}} \sum_{m=1}^M e^{j(\theta_m + 2\pi\nu_m t - 2\pi\tau_m f)}, \quad (2.10)$$

where  $\nu_m$  is a random Doppler shift, distributed according to a Doppler spectral density and  $\tau_m$  a random delay, distributed according to a power delay profile. The uniform distributed random phase  $\theta_m$  ensures circularly symmetry. Note that  $H(t, f)$  is a complex Gaussian process due to the central limit theorem. I further assume that the random variables  $\nu_m$  and  $\tau_m$  are independent, so that the time-frequency correlation function can be separated:

$$R_H(t - t', f - f') = r_{H_t}(t - t')r_{H_f}(f - f') \quad (2.11)$$

The time correlation  $r_{H_t}$  can be obtained as the inverse Fourier transformation of the Doppler spectral density while the frequency correlation  $r_{H_f}$  is given as the Fourier transformation of the power delay profile. A Jakes spectrum<sup>4</sup> therefore leads to the following correlation function [15]:

$$r_{H_t}(t - t') = J_0(2\pi\nu_{\max}(t - t')), \quad (2.12)$$

where  $J_0$  is the zeroth-order Bessel function. For a uniform distributed power delay profile<sup>5</sup>, the frequency correlation becomes:

$$r_{H_f}(f - f') = \frac{\sin(\pi\tau_{\max}(f - f'))}{\pi\tau_{\max}(f - f')}. \quad (2.13)$$

Note that the formulas derived in Chapter 3 and 4 do not need the as-

---

<sup>4</sup>  $\text{pdf}_\nu(\nu) = \frac{1}{\pi\nu_{\max}\sqrt{1-(\nu/\nu_{\max})^2}}$

<sup>5</sup>  $-\tau_{\max}/2 \leq \tau \leq \tau_{\max}/2$

sumptions of WSSUS and separability, but using them, makes the characterization of the channel easier (i.e., finding the required correlation matrices).

For numerical evaluations I assume a uniform distributed power delay profile and a Jakes Doppler spectrum so that Equation (2.12) and (2.13) can be used. The required WSSUS channel for the simulation can be approximated by applying Equation (2.10) to a finite, sufficient large, number of summations  $M$ . Matlab already provides a build in method for obtaining the delay realizations  $\tau_m$  whereas the Doppler shifts  $\nu_m$  have to be generated by applying the cos-function to an uniformly distributed<sup>6</sup> random variable and multiplying this result with  $\nu_{\max}$ .

## 2.2. Orthogonal Frequency Division Multiplexing

The basic principle of OFDM[12, 16] is to split a single high-data-rate stream into more mutually orthogonal low-data-rate streams, the so-called subcarriers. The basic pulse of subcarrier  $l$  can be interpreted as a frequency-shifted rectangular pulse:

$$\varphi_l(t) = \begin{cases} \frac{1}{\sqrt{T_s}} e^{j2\pi l \Delta f t} & \text{if } 0 \leq t \leq T_s \\ 0 & \text{otherwise} \end{cases}. \quad (2.14)$$

The function  $\varphi_l(t)$  builds an orthonormal basis<sup>7</sup> if the subcarrier spacing  $\Delta f$  multiplied by the OFDM symbol time  $T_s$  is a positive integer, whereby the most efficient time-bandwidth allocation can be obtained by choosing this integer number to one ( $\Delta f T_s = 1$ ). Figure 2.1 shows the frequency spectrum of three basic pulses which are sinc-shaped<sup>8</sup> functions due to the rectangular pulse in the time domain. The received symbols can be obtained by sampling this spectrum in the frequency domain whereas the sampled spectrum of subcarrier  $l_1$  shows spectral-nulls at all other positions  $l \neq l_1$ .

Orthogonality allows the transmission of several subcarriers at once while at the receiver side each subcarrier can be detected separately. The transmit

---

<sup>6</sup> between 0 and  $2\pi$

<sup>7</sup>  $\int_0^{T_s} \varphi_{l_1}(t) \varphi_{l_2}^*(t) dt = \delta[l_1 - l_2]$

<sup>8</sup>  $\frac{\sin(\pi f)}{\pi f}$

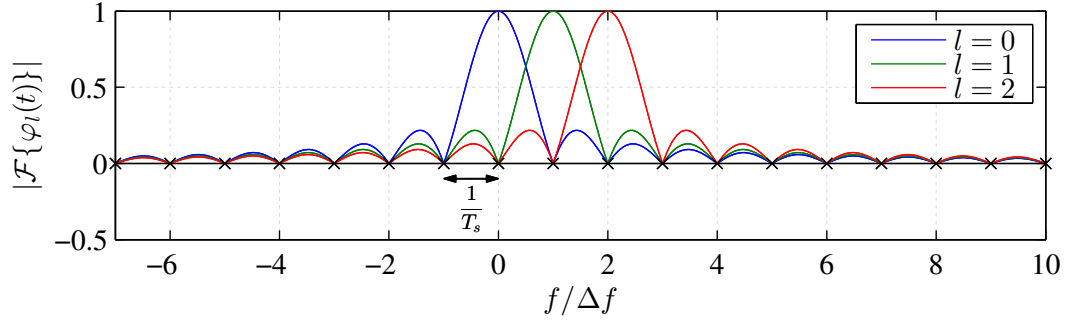


Figure 2.1: Frequency spectrum of three different basic pulses, sinc-shaped due to the rectangular pulse in the time domain, sampled spectrum of subcarrier  $l_1$  shows spectral-nulls at all other positions  $l \neq l_1 \Rightarrow$  orthogonal

signal can thus be written as:

$$s(t) = \sum_{k=0}^{K-1} \sum_{l=0}^{L-1} x_{l,k} \varphi_l(t - kT_s). \quad (2.15)$$

The complex data symbol  $x_{l,k}$  is usually chosen from a signal constellation such as Quadrature Amplitude Modulation (QAM). The inner sum represents one OFDM symbol at time-position  $k$  and consists of  $L$  individual subcarriers while the outer sum represents the successively transmission of  $K$  OFDM symbols.

If the transmit signal is corrupted by a frequency-selective channel, symbol  $k$  affects symbol  $k+1$ . This is called Inter Symbol Interference (ISI). To avoid ISI and to keep equalization simple, a special type of guard interval is used, the so-called cyclic prefix[17]. The basic pulse with cyclic prefix changes to:

$$\tilde{\varphi}_l(t) = \begin{cases} \frac{1}{\sqrt{T_s}} e^{j2\pi l \Delta f t} & \text{if } -T_{cp} \leq t \leq T_s \\ 0 & \text{otherwise} \end{cases}. \quad (2.16)$$

It is similar to Equation (2.14) but the pulse in (2.16) is extended by the length of the cyclic prefix  $T_{cp}$  so that the new OFDM symbol time with cyclic prefix becomes  $T_{\tilde{s}} = T_s + T_{cp}$ .

The received signal  $r(t)$  can be obtained as a convolution of the transmit signal  $s(t)$  and the channel impulse response  $h(t, \tau)$ :

$$r(t) = \sum_{k=0}^{K-1} \int_0^{\tau_{max}} h(t, \tau) \sum_{l=0}^{L-1} x_{l,k} \tilde{\varphi}_l(t - kT_{\tilde{s}} - \tau) d\tau. \quad (2.17)$$

I assume that the impulse response is limited between  $0 \leq h(t, \tau) \leq \tau_{max}$ , so that the received OFDM symbol  $k$  is time-limited by  $kT_s - T_{cp} \leq t \leq kT_s + T_s + \tau_{max}$ . In order to avoid ISI, the minimum length of the cyclic prefix  $T_{cp}$  therefore has to be  $\tau_{max}$ . For the useful time interval  $kT_s \leq t \leq kT_s + T_s$  and for  $T_{cp} \geq \tau_{max}$ , Equation (2.17) can be written as:

$$r(t) = \sum_{l=0}^{L-1} x_{l,k} \frac{1}{\sqrt{T_s}} e^{j2\pi l \Delta f (t - kT_s)} \underbrace{\int_0^{\tau_{max}} h(t, \tau) e^{-j2\pi l \Delta f \tau} d\tau}_{H(t, l\Delta f)}, \quad (2.18)$$

where  $H(t, l\Delta f)$  is a time-variant transfer function. Note that this is only true because of the special structure of the cyclic prefix. For example if zero padding instead of a cyclic prefix is used, the integral boundaries  $\int_0^{\tau_{max}}$  would become  $\int_0^t$  for  $t \leq \tau_{max}$  so that the receiver would experience a time-variant transfer function even if  $h(t, \tau)$  is constant over time.

The receiver removes the cyclic prefix and the demodulation is performed as follows:

$$y_{l,k} = \int_0^{T_s} r(t + kT_s) \varphi_l^*(t) dt, \quad (2.19)$$

and by including Equation (2.18)

$$y_{l,k} = \sum_{d=0}^{L-1} x_{d,k} \int_0^{T_s} H(t + kT_s, d\Delta f) \varphi_d(t) \varphi_l^*(t) dt. \quad (2.20)$$

If the channel is time-invariant, Equation (2.20) becomes a multiplication of the transfer function with the transmitted data symbol ( $y_{l,k} = H(kT_s, l\Delta f) x_{l,k}$ ), so that the channel equalization can be performed by a simple one-tap equalizer. The cyclic prefix therefore preserves the orthogonality of the basic pulses in a frequency-selective channel but has the drawback that the spectral efficiency is reduced (only  $T_s/(T_s + T_{cp})$  of the time is effectively used to transmit data). On the other hand, if the channel is time-variant, different subcarrier are no longer orthogonal.

The receiver can be implemented in the discrete-time domain. By sampling Equation (2.19) at  $t = n\Delta t = nT_s/N$ , the integral is replaced by a sum and can be rewritten as:

$$y_{l,k} = \frac{\Delta t}{\sqrt{T_s}} \sum_{n=0}^{N-1} r(n\Delta t + kT_s) e^{-j2\pi \frac{ln}{N}}, \quad (2.21)$$

which can be implemented in an efficient way by a Fast Fourier Transform (FFT). Similar Equation (2.20) becomes

$$y_{l,k} = \sum_{d=0}^{L-1} x_{d,k} \frac{1}{N} \sum_{n=0}^{N-1} H(n\Delta t + kT_s, d\Delta f) e^{-j2\pi \frac{l-d}{N} n}. \quad (2.22)$$

If the channel is time-invariant and  $N \geq L$ , different subcarriers remain orthogonal<sup>9</sup> so that the discrete-time receiver (Equation (2.21)) and the continuous-time receiver (Equation (2.19)) are equivalent ( $y_{l,k}$  is independent of  $N$ ). In a time-variant channel this is not the case because sampling generates copies in the frequency domain, causing additional interference.

The sampled transmit signal (Equation (2.15) for  $kT_s \leq t \leq kT_s + T_s$ ) can also be calculated in an efficient way:

$$s(n\Delta t + kT_s) = \frac{1}{\sqrt{T_s}} \sum_{l=0}^{L-1} x_{l,k} e^{j2\pi \frac{ln}{N}}. \quad (2.23)$$

This is usually implemented by a  $N$ -point Inverse Fast Fourier Transform (IFFT) where the missing  $N-L$  values are set to zero. However, because the basic pulses are not band limited the continuous signal  $s(t)$  can not be constructed by the samples  $s(n)$ . This means there is an error in Equation (2.22) which can be made arbitrary small by increasing the number of samples  $N$ . On the other hand, if the bandwidth of  $s(n)$  and  $h(t, \tau)$  is limited, the continuous-time convolution in (2.17) becomes a discrete-time convolution so that Equation (2.22) remains true but  $H(n, l)$  is now the DFT:  $H(n, l) = \sum_0^{m_{\max}} h(n, m) e^{-j2\pi \frac{lm}{N}}$ . The problem with this approach is that a band-limited signal is no longer time-limited and therefore resulting in an error because of ISI. Throughout this thesis I assume that these errors can be neglected.

Figure 2.2 shows a block diagram of the OFDM system discussed so far. By using Equation (2.22), the relationship between the received data symbols  $\mathbf{y}_k = [y_{1,k} \dots y_{L,k}]^T$  and the transmitted data symbols  $\mathbf{x}_k = [x_{1,k} \dots x_{L,k}]^T$  can be summarized by a matrix multiplication. Additionally, a random additive noise vector  $\mathbf{z}_k$  is included:

$$\mathbf{y}_k = \mathbf{D}_k \mathbf{x}_k + \mathbf{z}_k, \quad (2.24)$$

---

<sup>9</sup>  $\frac{1}{N} \sum_{n=0}^{N-1} e^{-j2\pi \frac{l-d}{N} n} = \delta[l-d]$

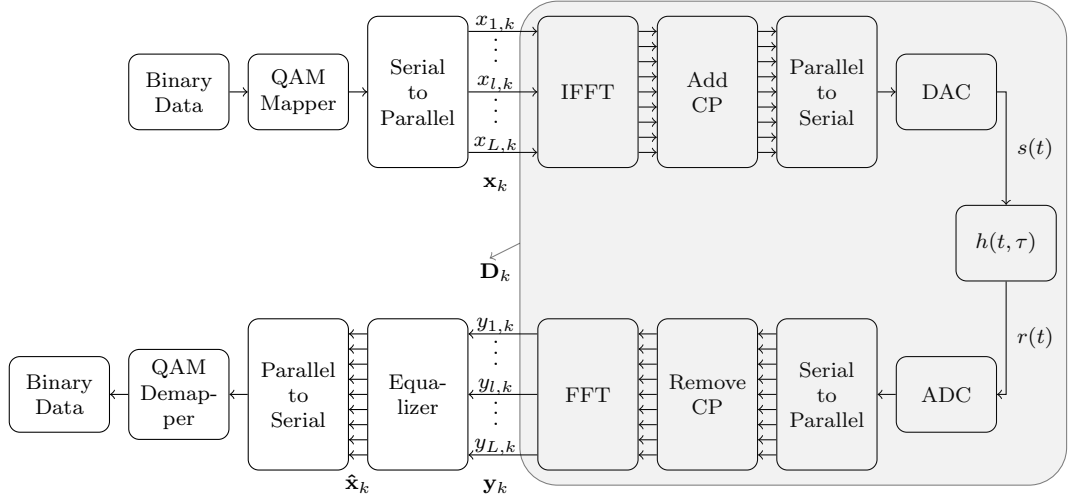


Figure 2.2: Block diagram of an OFDM system, the relationship between the received symbols and the transmitted symbols can be summarized by a matrix multiplication

with

$$(\mathbf{D}_k)_{l,d} = \frac{1}{N} \sum_{n=0}^{N-1} H[n + k(N + N_{cp}), d] e^{-j2\pi \frac{l-d}{N} n}. \quad (2.25)$$

The notation  $(\mathbf{D}_k)_{l,d}$  denotes the matrix entry in the  $l$ -th row and  $d$ -th column, while the variable  $N_{cp}$  is the length of the cyclic prefix in the discrete-time domain  $(\frac{T_{cp}}{\Delta t})$ . Note that  $\mathbf{D}_k$  can be interpreted as a rearranged version of the discrete-Doppler-variant transfer function and that the diagonal elements are simply the piecewise time averages of  $H[n, l]$ . Furthermore if the channel is time-invariant,  $\mathbf{D}_k$  becomes a diagonal matrix. The noise vector is assumed to be jointly complex Gaussian with zero mean:  $\mathbf{z}_k \sim \mathcal{CN}(0, \mathbf{R}_{\mathbf{z}_k})$ .

## 3. Inter-Carrier Interference

The effect of ICI can be best understood by examining the basic pulses in the frequency domain, see Figure 2.1. Suppose the channel induces a single frequency-shift. The basic pulses are then shifted in the frequency domain which, sampled at the original subcarrier positions, causes two effects: First, the signal power is reduced and second, subcarriers interfere each other whereas this interference becomes smaller the farther away the subcarriers are. In reality, however, the channel consists of not only one frequency-shift but many frequency-shifts simultaneously whose statistic is determined by the Doppler-spectral density.

### 3.1. Inter-Carrier Interference Power

For the analytical derivation of the ICI effects I use the following assumptions:

- Channel, noise, and data symbols are statistically independent from each other
- The mean channel power is normalized to one:  $\mathbb{E} \{|H[n, l]|^2\} = 1$
- The data symbols are statistically independent, have zero mean, and are normalized to have mean power one:  $\mathbb{E} \{x_{l_1, k_1} x_{l_2, k_2}^*\} = \delta[l_1 - l_2] \delta[k_1 - k_2]$

Equation (2.24) can be split into a signal-part  $y_{S_{l,k}}$ , an ICI-part  $y_{ICI_{l,k}}$ , and a noise-part  $z_{l,k}$ :

$$y_{l,k} = \underbrace{(\mathbf{D}_k)_{l,l} x_{l,k}}_{y_{S_{l,k}}} + \underbrace{\sum_{\substack{d=1 \\ d \neq l}}^L (\mathbf{D}_k)_{l,d} x_{d,k}}_{y_{ICI_{l,k}}} + z_{l,k}, \quad (3.1)$$

Because of the assumptions stated above, the received data symbol power  $\mathbb{E}\{y_{l,k}y_{l,k}^*\}$  is given as a summation of the signal power  $P_{S_{l,k}}$ , the ICI power  $P_{ICI_{l,k}}$ , and the noise power  $P_{\text{noise}_{l,k}}$ :

$$\mathbb{E}\{y_{l,k}y_{l,k}^*\} = \underbrace{\mathbb{E}\left\{\left|(\mathbf{D}_k)_{l,l}\right|^2\right\}}_{P_{S_{l,k}}} + \underbrace{\sum_{\substack{d=1 \\ d \neq l}}^L \mathbb{E}\left\{\left|(\mathbf{D}_k)_{l,d}\right|^2\right\}}_{P_{ICI_{l,k}}} + \underbrace{\mathbb{E}\{z_{l,k}^2\}}_{P_{\text{noise}_{l,k}}}, \quad (3.2)$$

with

$$\mathbb{E}\left\{\left|(\mathbf{D}_k)_{l,d}\right|^2\right\} = \frac{1}{N^2} \sum_{n_1=0}^{N-1} \sum_{n_2=0}^{N-1} \mathbb{E}\{H[n_1, d]H^*[n_2, d]\} e^{-j2\pi \frac{l-d}{N}(n_1-n_2)}. \quad (3.3)$$

The signal and ICI powers depend only on the autocorrelation function  $\mathbb{E}\{H(n_1, d)H^*(n_2, d)\}$ , the number of subcarriers  $L$ , and the number of samples  $N$ . For infinite many subcarriers and a given time autocorrelation function, a closed form solution for the signal power can be found as [2]:

$$P_{S_{\text{uniform}}} = \frac{\cos(2\pi\nu_{\max}T_s) + 2\pi\nu_{\max}T_s \text{Si}(2\pi\nu_{\max}T_s) - 1}{2(\pi\nu_{\max}T_s)^2}, \quad (3.4a)$$

$$P_{S_{\text{Jakes}}} = {}_1F_2\left(\frac{1}{2}; \frac{3}{2}, 2; -(\pi\nu_{\max}T_s)^2\right). \quad (3.4b)$$

A uniform distributed Doppler spectral density is assumed for the signal power  $P_{S_{\text{uniform}}}$  and a Jakes Doppler spectrum for  $P_{S_{\text{Jakes}}}$ . The functions  $\text{Si}(\cdot)$  and  ${}_1F_2(\cdot)$  are the sine integral function respectively the generalized hypergeometric function. Note that the signal power depends only on the normalized maximum Doppler shift  $\nu_{\max}T_s = \frac{\nu_{\max}}{\Delta f}$ . Because infinite many subcarriers are assumed, the law of conservation of energy ( $P_S + P_{\text{ICI}} = 1$ ) can be applied, so that the

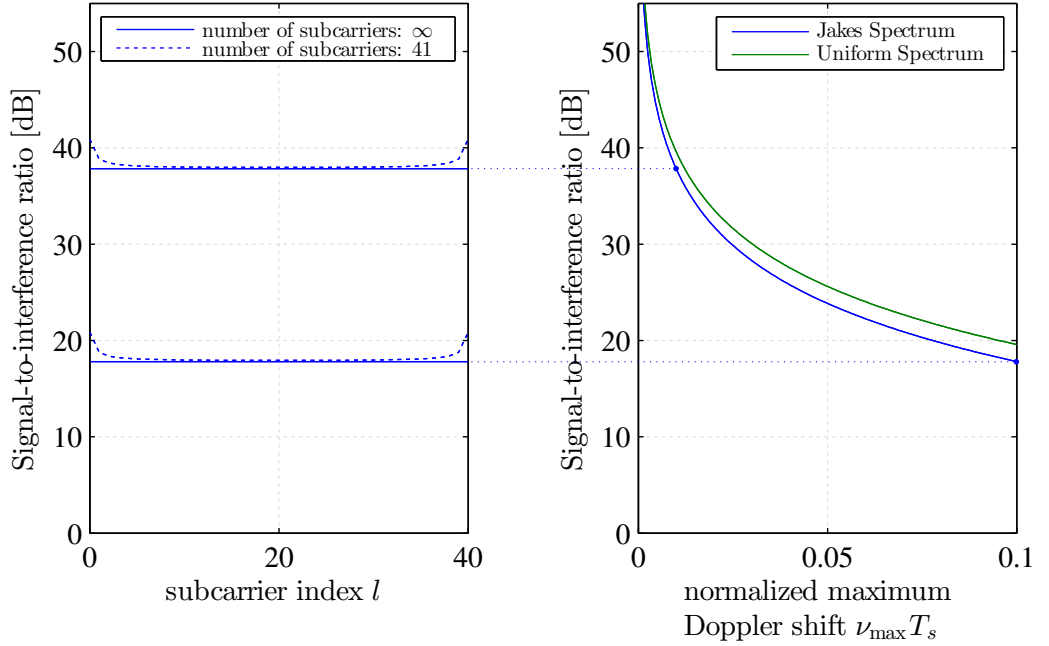


Figure 3.1: Signal-to-Interference Ratio as a function of subcarrier index respectively Doppler shift: SIR is relatively high so that in most cases ICI can be neglected, SIR of the first and last subcarrier is approximately 3 dB higher

ICI power is finally given as:

$$P_{\text{ICI}_{\text{uniform}}} = P_{\text{S}_{\text{uniform}}} - 1, \quad (3.5a)$$

$$P_{\text{ICI}_{\text{Jakes}}} = P_{\text{S}_{\text{Jakes}}} - 1. \quad (3.5b)$$

The right part of Figure 3.1 shows the Signal-to-Interference Ratio (SIR) for infinite many subcarriers (Equation (3.4) and (3.5)). This ratio is usually very high so that in most cases the ICI can be neglected compared to the noise. Consider for example LTE ( $\Delta f = 15$  kHz) at 2.5 GHz. For a SIR smaller than 20 dB, the velocity has to be larger than 500 km/h ( $\nu_{\max} T_s = 0.08$ ). The left figure compares the case of finite (Equation (3.2),  $L = 41, N = 410$ ) to infinite many subcarriers. Since the first and last subcarriers have interferers only at one side, the SIR is approximately 3 dB higher compared to the closed form solution. Furthermore, it can be seen that the SIR ratio at the middle subcarrier coincide with the closed form solution because only the few nearest neighboring subcarriers have a significant effect on the ICI.

### 3.2. L-Dimensional Probability Density Function

I now calculate the pdf of the ICI. As a first step, Equation (2.24) has to be rewritten in a form that is more suitable for a statistical analysis. For this, I need two new variables, the transfer-function matrix  $\mathbf{H}_k$ , defined for  $n = 0 \dots N - 1$  and  $d = 0 \dots L - 1$  as follows:

$$(\mathbf{H}_k)_{n,d} = H[n + k(N + N_{cp}), d], \quad (3.6)$$

and a new data symbol matrix  $\tilde{\mathbf{X}}_k$ :

$$\tilde{\mathbf{X}}_k = \tilde{\mathbf{X}}_{S_k} + \tilde{\mathbf{X}}_{ICI_k} = \mathbf{x}_k^T \otimes \mathbf{I}_L, \quad (3.7)$$

where  $\mathbf{I}_L$  is the identity matrix of size  $L$ . The data symbols that affect the ICI part are represented by  $\tilde{\mathbf{X}}_{ICI_k}$  which can be obtained from  $\tilde{\mathbf{X}}_k$  by setting the columns  $i(L + 1)$  for  $i = 0 \dots L - 1$  to zero. On the other hand,  $\tilde{\mathbf{X}}_{S_k}$  consist of the data symbols that affects only the signal part.

It is then possible to find a non-square block diagonal matrix  $\mathbf{W}$  (see Appendix A) so that  $\text{vec}\{\mathbf{D}_k\} = \mathbf{W}\text{vec}\{\mathbf{H}_k\}$ . Including  $\tilde{\mathbf{X}}_{S_k}$  and  $\tilde{\mathbf{X}}_{ICI_k}$ , Equation (2.24) can be rewritten as:

$$\mathbf{y}_k = \underbrace{\tilde{\mathbf{X}}_{S_k} \mathbf{W} \text{vec}\{\mathbf{H}_k\}}_{\mathbf{y}_{S_k}} + \underbrace{\tilde{\mathbf{X}}_{ICI_k} \mathbf{W} \text{vec}\{\mathbf{H}_k\}}_{\mathbf{y}_{ICI_k}} + \mathbf{z}_k, \quad (3.8)$$

whereas  $\mathbf{y}_{S_k}$  represents the signal part of the received symbol and  $\mathbf{y}_{ICI_k}$  the ICI part.

The next step consists of calculating the ICI pdf conditioned on  $\mathbf{x}_k$ . Because the elements of the transfer-function matrix  $\mathbf{H}$  are assumed to be jointly complex Gaussian:  $\text{vec}\{\mathbf{H}\} \sim \mathcal{CN}(0, \mathbf{R}_{\text{vec}\{\mathbf{H}_k\}})$  and a linear transformation of such a distribution remains jointly complex Gaussian [18], the conditional ICI given  $\mathbf{x}_k$  is also a jointly complex Gaussian variable:  $\mathbf{y}_{ICI_k} | \mathbf{x}_k \sim \mathcal{CN}(0, \mathbf{R}_{\mathbf{y}_{ICI_k} | \mathbf{x}_k})$ . The required ICI correlation matrix conditioned on  $\mathbf{x}_k$  can be found as:

$$\mathbf{R}_{\mathbf{y}_{ICI_k} | \mathbf{x}_k} = \tilde{\mathbf{X}}_{ICI_k} \underbrace{\mathbf{W} \mathbf{R}_{\text{vec}\{\mathbf{H}_k\}} \mathbf{W}^H}_{\mathbf{R}_{\text{vec}\{\mathbf{D}_k\}}} \tilde{\mathbf{X}}_{ICI_k}^H, \quad (3.9)$$

whereas Appendix B provides an expression for the correlation matrix  $\mathbf{R}_{\text{vec}\{\mathbf{H}_k\}}$ .

Finally, the unconditional joint pdf of  $\mathbf{y}_{ICI_k}$  can be found by applying the law

of total probability. Since the data symbols are statistically independent and equally likely, the unconditional pdf can be obtained as the mean of every possible conditional pdf:

$$\text{pdf}_{\mathbf{y}_{\text{ICI}_k}}(\mathbf{y}_{\text{ICI}_k}) = \frac{1}{|\mathcal{X}|} \sum_{\mathbf{x}_k \in \mathcal{X}} \frac{1}{\pi^L \det(\mathbf{R}_{\mathbf{y}_{\text{ICI}}|\mathbf{x}_k})} \exp\left(-\mathbf{y}_{\text{ICI}_k}^H \mathbf{R}_{\mathbf{y}_{\text{ICI}}|\mathbf{x}_k}^{-1} \mathbf{y}_{\text{ICI}_k}\right), \quad (3.10)$$

where  $\mathcal{X}$  represents the set of possible transmit data symbols and  $|\mathcal{X}|$  its cardinality (e.g. for m-QAM,  $|\mathcal{X}| = m^L$ ).

### 3.3. One-Dimensional Probability Density Function

Next, I reduce the  $L$ -dimensional pdf (Equation (3.10)) to one-dimension. For subcarrier  $l$ , the conditional ICI part given some data symbol<sup>1</sup>  $\mathbf{x}_k$  is also Gaussian distributed  $y_{\text{ICI}_{l,k}}|\mathbf{x}_k \sim \mathcal{CN}(0, \sigma_{y_{\text{ICI}_{l,k}}|\mathbf{x}_k}^2)$ . The conditional variance  $\sigma_{y_{\text{ICI}_{l,k}}|\mathbf{x}_k}^2$  can be found either as the  $l$ -th diagonal element of the conditional correlation matrix  $\mathbf{R}_{\mathbf{y}_{\text{ICI}}|\mathbf{x}_k}$  or by direct calculation using an appropriate (correlation) matrix  $\mathbf{M}_{\text{ICI}_{l,k}}$ :

$$\sigma_{y_{\text{ICI}_{l,k}}|\mathbf{x}_k}^2 = \mathbf{x}_k^T \mathbf{M}_{\text{ICI}_{l,k}} \mathbf{x}_k^*. \quad (3.11)$$

The matrix  $\mathbf{M}_{\text{ICI}_{l,k}}$  can be obtained by setting the  $l$ -th column and  $l$ -th row of the correlation matrix  $\mathbf{R}_{\text{vec}\{(\mathbf{D}_k)_{l,1\dots L}\}}$  to zero.

Similar to Equation (3.10), the one dimensional unconditional pdf of the ICI part can then be found as:

$$\text{pdf}_{y_{\text{ICI}_{l,k}}} (y_{\text{ICI}_{l,k}}) = \frac{1}{|\mathcal{X}|} \sum_{\mathbf{x}_k \in \mathcal{X}} \frac{1}{\pi \sigma_{y_{\text{ICI}_{l,k}}|\mathbf{x}_k}^2} \exp\left(-\frac{|y_{\text{ICI}_{l,k}}|^2}{\sigma_{y_{\text{ICI}_{l,k}}|\mathbf{x}_k}^2}\right). \quad (3.12)$$

According to Equation (3.12), the ICI part becomes Gaussian distributed only if the variance  $\sigma_{y_{\text{ICI}_{l,k}}|\mathbf{x}_k}^2$  is constant over different data symbols  $\mathbf{x}_k$  i.e. the variance of  $\sigma_{y_{\text{ICI}_{l,k}}|\mathbf{x}_k}^2$  has to be zero. Using the assumption<sup>2</sup>  $\mathbb{E}\{x_{d,k}x_{d,k}\} = 0$ , the

---

<sup>1</sup> for consistency, I use  $\mathbf{x}_k$  even if the ICI part of subcarrier  $l$  is independent of  $x_{l,k}$

<sup>2</sup> fulfilled e.g. for m-QAM

variance can be written as:

$$\begin{aligned} \text{Var} \left\{ \sigma_{y_{\text{ICI},k}}^2 \right\} = & \sum_{d=0}^{L-1} \left| (\mathbf{M}_{\text{ICI},k})_{d,d} \right|^2 \left( \mathbb{E} \left\{ x_{d,k} x_{d,k}^* x_{d,k} x_{d,k}^* \right\} - 1 \right) + \\ & \sum_{d_1=0}^{L-1} \sum_{\substack{d_2=0 \\ d_2 \neq d_1}}^{L-1} \left| (\mathbf{M}_{\text{ICI},k})_{d_1,d_2} \right|^2, \end{aligned} \quad (3.13)$$

and gives, together with the ICI power  $P_{\text{ICI},k} = \mathbb{E} \{ \sigma_{y_{\text{ICI},k}}^2 \}$ , a rough estimation of how much the pdf of the ICI differs from a Gaussian distribution. If every possible data symbol  $x_{l,k}$  has energy one (e.g. 4-QAM), the expected value  $\mathbb{E} \{ x_{d,k} x_{d,k}^* x_{d,k} x_{d,k}^* \}$  becomes also one. For higher modulation orders this value is higher. Therefore, the ICI becomes Gaussian distributed only if every data symbol has energy one and the non-diagonal elements of  $\mathbf{M}_{\text{ICI},k}$  are zero, i.e. the transfer function for different subcarrier positions has to be uncorrelated, which is highly unrealistic.

The ICI power can also be calculated using the matrix  $\mathbf{M}_{\text{ICI},k}$ :

$$P_{\text{ICI},k} = \mathbb{E} \left\{ \sigma_{y_{\text{ICI},k}}^2 \right\} = \sum_{d=1}^L (\mathbf{M}_{\text{ICI},k})_{d,d}. \quad (3.14)$$

For infinite many subcarriers, the ICI becomes Gaussian distributed if:

$$\lim_{L \rightarrow \infty} \left( \frac{\sqrt{\text{Var} \left\{ \sigma_{y_{\text{ICI},k}}^2 \right\}}}{\mathbb{E} \left\{ \sigma_{y_{\text{ICI},k}}^2 \right\}} \right) = 0. \quad (3.15)$$

Because the ICI power is limited (Equation (3.5)) and an additional subcarrier can only increase the variance (Equation (3.13)), Equation (3.15) does not approach to zero, i.e. the ICI is not Gaussian distributed even in the case of infinite many subcarriers.

For a high number of subcarriers, the sum in Equation (3.12) can be replaced by an integral:

$$\text{pdf}_{y_{\text{ICI},k}}(y_{\text{ICI},k}) = \int_0^\infty \left( \text{pdf}_{\sigma_{y_{\text{ICI},k}}^2}(\sigma^2) \right) \frac{1}{\pi \sigma^2} \exp \left( -\frac{|y_{\text{ICI},k}|^2}{\sigma^2} \right) d\sigma^2. \quad (3.16)$$

Figure 3.2 gives a numerical example of the ICI pdf for the middle sub-

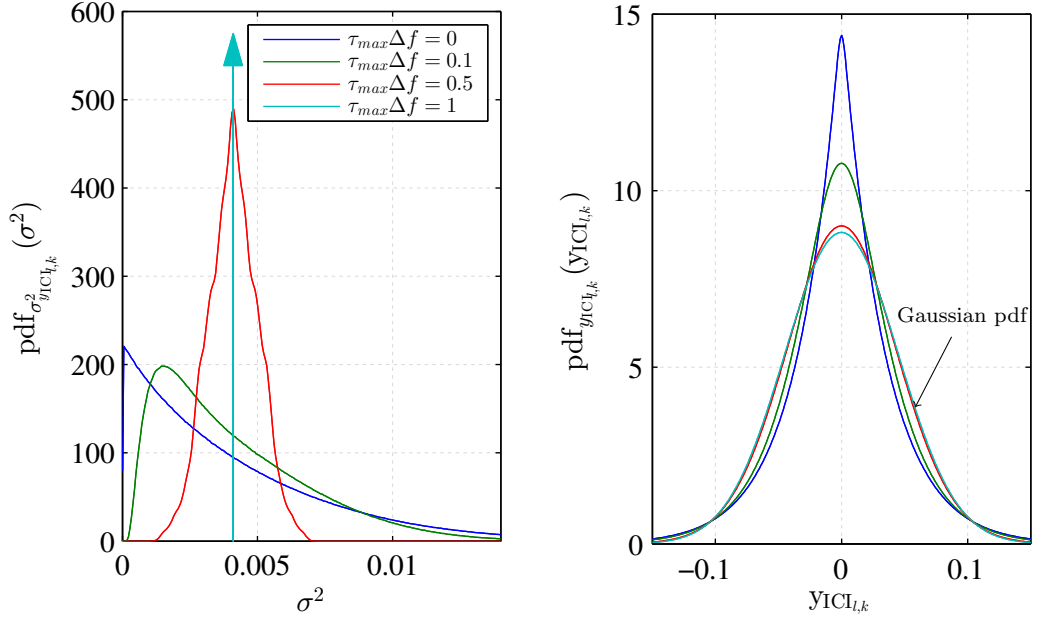


Figure 3.2: pdf of the ICI-power  $\sigma^2_{y_{ICI_{l,k}}}$  and the pdf of the ICI  $y_{ICI_{l,k}}$ , only for  $\tau_{max}\Delta f = 1$  Gaussian distributed

carrier, 4-QAM, 600 subcarriers, 1024 samples, Jakes Doppler spectrum ( $\nu_{max}T_s = 0.05$ ) and a uniform power delay profile. The exact calculation of the one-dimensional ICI pdf, according to Equation (3.12), would require  $4^{600}$  summations which is not feasible. I therefore approximate the function by the method of Monte Carlo. The high number of subcarriers allows an approximation of the probability mass function of  $\sigma^2_{y_{ICI_{l,k}}}$  by a pdf (Equation (3.16)). Note that every curve in the left figure has the same expected value. The variances of the curves in the right figure are therefore also equal. Furthermore it can be seen that the higher the correlation of the transfer function for different subcarrier positions, the more the ICI pdf differs from a Gaussian distribution (extreme case: flat fading,  $\tau_{max}\Delta f = 0$ ). For the case of uncorrelatedness ( $\tau_{max}\Delta f = 1$ ) the ICI is indeed Gaussian distributed<sup>3</sup>.

<sup>3</sup> for 4-QAM

## 4. Pilot-Symbol-Aided Channel Estimation

Recovering the transmitted bit-stream is the ultimate goal of every telecommunication system. In the absence of noise and if the channel is perfectly known, the transmitted data symbol  $\mathbf{x}_k$  can be perfectly estimated by multiplication of the received data symbol  $\mathbf{y}_k$  with the inverse of the matrix  $\mathbf{D}_k$ :

$$\hat{\mathbf{x}}_k = \mathbf{x}_k = \mathbf{D}_k^{-1} \mathbf{y}_k. \quad (4.1)$$

Equation (4.1) has two practical problems: First, for each received OFDM symbol a matrix inversion has to be performed and second, the channel is not perfectly known and has to be estimated. I therefore consider the ICI part as an additional noise term so that Equation (2.24) can be written as:

$$y_{l,k} = h_{l,k} x_{l,k} + y_{\text{ICI}_{l,k}} + z_{l,k}. \quad (4.2)$$

The channel  $h_{l,k}$  can be found as the  $l$ -th diagonal element of the OFDM matrix  $\mathbf{D}_k$ . Dividing Equation (4.2) by  $h_{l,k}$  leads to the zero forcing equalization of  $y_{l,k}$  and delivers an estimate of the transmitted data symbol  $x_{l,k}$ :

$$\hat{x}_{l,k} = \frac{y_{l,k}}{h_{l,k}} = x_{l,k} + \frac{y_{\text{ICI}_{l,k}} + z_{l,k}}{h_{l,k}}. \quad (4.3)$$

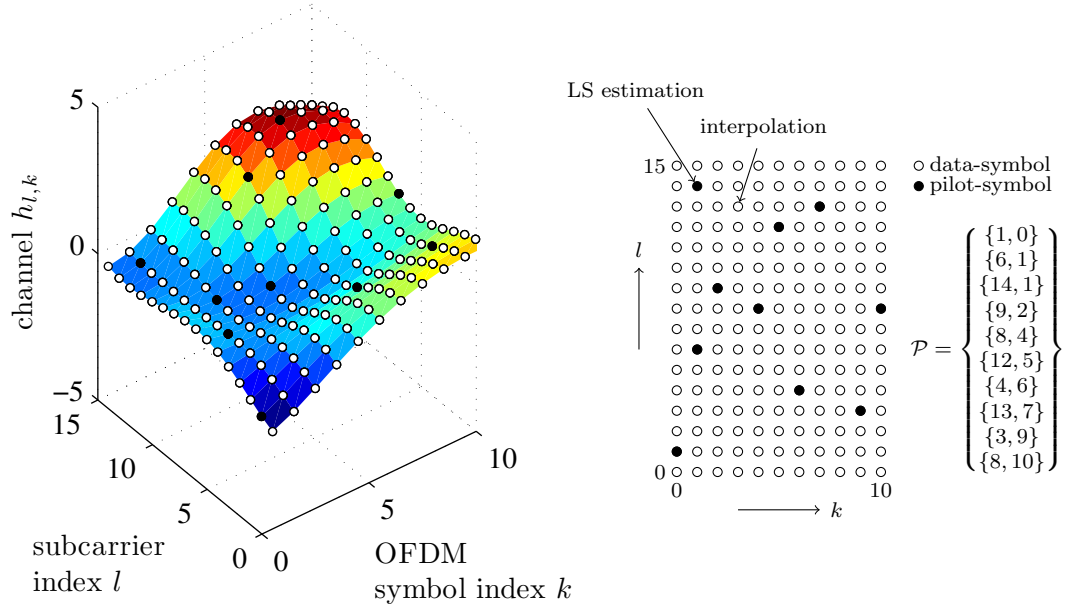


Figure 4.1: Pilot-Symbol-Aided Channel Estimation, known symbols are used to estimate the channel at pilot position, the channel at data position is estimated through interpolation

In reality, however, the channel  $h_{l,k}$  is not known and has to be estimated, so that Equation (4.3) becomes:

$$\hat{x}_{l,k} = \frac{y_{l,k}}{\hat{h}_{l,k}} = x_{l,k} \frac{h_{l,k}}{\hat{h}_{l,k}} + \frac{y_{\text{ICI}_{l,k}} + z_{l,k}}{\hat{h}_{l,k}}. \quad (4.4)$$

In this thesis, the channel estimation is performed by “pilot-symbol-aided channel estimation” where, in a first step, known symbols are used to estimate the channel at pilot position. In a second step, the channel at data position is estimated through interpolation (see Figure 4.1).

The estimates at pilot position are obtained by a Least Squares (LS)-estimation which minimizes the error of the  $L^2$  norm and requires no statistical knowledge:

$$\hat{h}_{l,k}^{\text{LS}} = \arg \min_{\tilde{h}_{l,k}} \|y_{l,k} - \tilde{h}_{l,k} x_{l,k}\|_2^2 = \frac{y_{l,k}}{x_{l,k}}. \quad (4.5)$$

Equation (4.5) shows that the transmitted data-symbol  $x_{l,k}$  needs to be known at the receiver and can not be used to transmit information. The channel estimates at data position can then be obtained as a weighted average of the

known LS estimates:

$$\hat{h}_{l,k} = \sum_{\{l_p, k_p\} \in \mathcal{P}} (\mathbf{w}_{l,k}^*)_{\{l_p, k_p\}} \frac{y_{l_p, k_p}}{x_{l_p, k_p}}. \quad (4.6)$$

The set  $\mathcal{P}$  is a collection of the two-Dimensional (2D) pilot position indexes and  $|\mathcal{P}|$  represents the overall number of pilot symbols. Equation (4.6) can also be written in vector notation:

$$\hat{h}_{l,k} = \mathbf{w}_{l,k}^H \hat{\mathbf{h}}_{\mathcal{P}}^{\text{LS}}. \quad (4.7)$$

The vector  $\hat{\mathbf{h}}_{\mathcal{P}}^{\text{LS}}$  consists of the vectorized LS estimates at pilot positions and the weighting vector  $\mathbf{w}_{l,k}^H$  depends on the interpolation method (e.g., MMSE, linear, spline, low-pass).

In order to compare different interpolation methods ( $\mathbf{w}_{l,k}^H$ ), I derive the MSE as well as the BEP for arbitrary weighting vectors. I make the following assumptions regarding the pilot-symbols:

- Every pilot-symbol has unit magnitude:  $|x_{l_p, k_p}| = 1$  for  $\{l_p, k_p\} \in \mathcal{P}$
- The pilot-symbols are random, statistically independent and of zero mean.
- Known pilot-symbols have no significant effect on the statistic of the ICI.

The last assumption guarantees that the MMSE channel estimation is independent of concrete pilots symbols.

### 4.1. Mean Squared Error

The MSE of the channel estimate  $\hat{h}_{l,k}$  can be found as:

$$\text{MSE}_{l,k}(\mathbf{w}_{l,k}^H) = \mathbb{E} \left\{ \|h_{l,k} - \hat{h}_{l,k}\|_2^2 \right\} \quad (4.8)$$

$$= P_{S_{l,k}} - \mathbf{w}_{l,k}^H \mathbf{R}_{h_{l,k}, \hat{\mathbf{h}}_{\mathcal{P}}^{\text{LS}}}^H - \mathbf{R}_{h_{l,k}, \hat{\mathbf{h}}_{\mathcal{P}}^{\text{LS}}} \mathbf{w}_{l,k} + \mathbf{w}_{l,k}^H \mathbf{R}_{\hat{\mathbf{h}}_{\mathcal{P}}^{\text{LS}}} \mathbf{w}_{l,k} \quad (4.9)$$

$$= \left( \mathbf{w}_{l,k}^H - \mathbf{R}_{h_{l,k}, \hat{\mathbf{h}}_{\mathcal{P}}^{\text{LS}}} \mathbf{R}_{\hat{\mathbf{h}}_{\mathcal{P}}^{\text{LS}}}^{-1} \right) \mathbf{R}_{\hat{\mathbf{h}}_{\mathcal{P}}^{\text{LS}}} \left( \mathbf{w}_{l,k} - \mathbf{R}_{\hat{\mathbf{h}}_{\mathcal{P}}^{\text{LS}}}^{-1} \mathbf{R}_{h_{l,k}, \hat{\mathbf{h}}_{\mathcal{P}}^{\text{LS}}}^H \right) + P_{S_{l,k}} - \mathbf{R}_{h_{l,k}, \hat{\mathbf{h}}_{\mathcal{P}}^{\text{LS}}} \mathbf{R}_{\hat{\mathbf{h}}_{\mathcal{P}}^{\text{LS}}}^{-1} \mathbf{R}_{h_{l,k}, \hat{\mathbf{h}}_{\mathcal{P}}^{\text{LS}}}^H. \quad (4.10)$$

In Equation (4.10) the method of “completing the square” was used which gives immediately the MMSE channel estimation because the correlation matrix

$\mathbf{R}_{\hat{\mathbf{h}}_{\mathcal{P}}^{\text{LS}}}$  is positive definite<sup>1</sup> (and therefore nonsingular). The MMSE weighting vector can thus be written as:

$$(\mathbf{w}_{l,k}^H)^{\text{MMSE}} = \arg \min_{\mathbf{w}_{l,k}^H} \text{MSE}_{l,k}(\mathbf{w}_{l,k}^H) = \mathbf{R}_{h_{l,k}, \hat{\mathbf{h}}_{\mathcal{P}}^{\text{LS}}} \mathbf{R}_{\hat{\mathbf{h}}_{\mathcal{P}}^{\text{LS}}}^{-1}, \quad (4.11)$$

and was already derived in [19] who used the orthogonal projection theorem instead of the “completing the square” approach.

The calculation of the MSE requires the correlation matrix  $\mathbf{R}_{\hat{\mathbf{h}}_{\mathcal{P}}^{\text{LS}}}$  whose elements are given by:

$$\begin{aligned} \mathbb{E} \left\{ \hat{h}_{l_1, k_1}^{\text{LS}} (\hat{h}_{l_2, k_2}^{\text{LS}})^* \right\} &= \sum_{d_1=1}^L \sum_{d_2=1}^L \mathbb{E} \left\{ (\mathbf{D}_{k_1})_{l_1, d_1} (\mathbf{D}_{k_2})_{l_2, d_2}^* \right\} \mathbb{E} \left\{ \frac{x_{d_1, k_1}}{x_{l_1, k_1}} \frac{x_{d_2, k_2}^*}{x_{l_2, k_2}^*} \right\} + \mathbb{E} \left\{ \frac{z_{l_1, k_1} z_{l_2, k_2}^*}{x_{l_1, k_1} x_{l_2, k_2}^*} \right\} \\ &= \mathbb{E} \left\{ (\mathbf{D}_{k_1})_{l_1, l_1} (\mathbf{D}_{k_2})_{l_2, l_2}^* \right\} + (P_{\text{ICI}_{l_1, k_1}} + P_{\text{noise}_{l_1, k_1}}) \delta[l_1 - l_2] \delta[k_1 - k_2], \end{aligned} \quad (4.12)$$

$$= \mathbb{E} \left\{ (\mathbf{D}_{k_1})_{l_1, l_1} (\mathbf{D}_{k_2})_{l_2, l_2}^* \right\} + (P_{\text{ICI}_{l_1, k_1}} + P_{\text{noise}_{l_1, k_1}}) \delta[l_1 - l_2] \delta[k_1 - k_2], \quad (4.13)$$

so that the correlation matrix becomes:

$$\mathbf{R}_{\hat{\mathbf{h}}_{\mathcal{P}}^{\text{LS}}} = \mathbf{R}_{\mathbf{h}_{\mathcal{P}}} + \text{diag}(\mathbf{p}_{\text{ICI}_{\mathcal{P}}} + \mathbf{p}_{\text{noise}_{\mathcal{P}}}), \quad (4.14)$$

The vectors  $\mathbf{p}_{\text{ICI}_{\mathcal{P}}}, \mathbf{p}_{\text{noise}_{\mathcal{P}}} \in \mathbb{R}^{|\mathcal{P}| \times 1}$  consists of the vectorized ICI- respectively noise-powers at pilot position and the  $\text{diag}(\cdot)$  operator creates a diagonal matrix out of a vector. Equation (4.14) shows that even if the noise correlation matrices  $\mathbf{R}_{\mathbf{y}_{\text{ICI}_k}}$  and  $\mathbf{R}_{\mathbf{z}_k}$  are non-diagonal matrices, the noise terms of different LS channel estimates are uncorrelated.

In a similar way the elements of the cross-correlation matrix  $\mathbf{R}_{h_{l,k}, \hat{\mathbf{h}}_{\mathcal{P}}^{\text{LS}}}$  can be found as:

$$\mathbb{E} \left\{ h_{l_1, k_1} (\hat{h}_{l_2, k_2}^{\text{LS}})^* \right\} = \sum_{d_2=1}^L \mathbb{E} \left\{ (\mathbf{D}_{k_1})_{l_1, l_1} (\mathbf{D}_{k_2})_{l_2, d_2}^* \right\} \mathbb{E} \left\{ \frac{x_{d_2, k_2}^*}{x_{l_2, k_2}^*} \right\} + \mathbb{E} \left\{ (\mathbf{D}_{k_1})_{l_1, l_1} z_{l_2, k_2}^* \right\} \quad (4.15)$$

$$= \mathbb{E} \left\{ (\mathbf{D}_{k_1})_{l_1, l_1} (\mathbf{D}_{k_2})_{l_2, l_2}^* \right\}, \quad (4.16)$$

---

<sup>1</sup> if the elements of  $\hat{\mathbf{h}}_{\mathcal{P}}^{\text{LS}}$  are linearly independent

and again in matrix notation

$$\mathbf{R}_{h_{l,k}, \hat{\mathbf{h}}_{\mathcal{P}}^{\text{LS}}} = \mathbf{R}_{h_{l,k}, \mathbf{h}_{\mathcal{P}}}. \quad (4.17)$$

Appendix B provides a compact method of calculating the correlation matrix  $\mathbf{R}_{\mathbf{h}_{\mathcal{P}}}$  and the cross-correlation matrix  $\mathbf{R}_{h_{l,k}, \mathbf{h}_{\mathcal{P}}}$  for the case of WSSUS and a separable time-frequency correlation function. Note that, due to vectorization of the LS estimates, these matrices do not show a “clear” time-frequency structure.

## 4.2. Bit Error Probability

Although the MSE (Equation (4.8)) allows a comparison of different interpolation methods, the BEP is a more intuitive measure. I therefore calculate the BEP for an arbitrary weighting vector  $\mathbf{w}_{l,k}^H$ . This calculation is based on [20] where in particular I make use of the following lemma:

**Lemma 1.** *Let  $X$  and  $Y$  be zero mean, correlated complex-valued Gaussian random variables, then*

$$\Pr(\Re\{XY^*\} < 0) = \frac{1}{2} \left[ 1 - \frac{\Re\{\mathbb{E}\{XY^*\}\}}{\sqrt{\mathbb{E}\{XX^*\}\mathbb{E}\{YY^*\} - (\Im\{\mathbb{E}\{XY^*\}\})^2}} \right] \quad (4.18)$$

$$\Pr(\Im\{XY^*\} < 0) = \frac{1}{2} \left[ 1 - \frac{\Im\{\mathbb{E}\{XY^*\}\}}{\sqrt{\mathbb{E}\{XX^*\}\mathbb{E}\{YY^*\} - (\Re\{\mathbb{E}\{XY^*\}\})^2}} \right] \quad (4.19)$$

For the calculation of the BEP I further assume that:

- The channel  $h_{l,k}$  and the noise  $z_{l,k}$  are Gaussian random variable (Rayleigh fading)
- The noise power  $P_{\text{noise}_{l,k}}$  is much larger than the ICI power  $P_{\text{ICI}_{l,k}}$

The last assumption ensures that the non-Gaussian ICI (see Chapter 3) can be neglect and therefore Lemma 1 applied.

Figure 4.2 shows the signal constellation for 4-QAM and 16-QAM. The mapping of the estimated data symbol  $\hat{x}_{l,k}$  to the unknown bit stream (demapping) is performed by minimizing the euclidean distance. The decision boundaries for 4-QAM are therefore the real and imaginary axis and for 16-QAM the real and imaginary axis shifted by 0 and  $\pm \frac{2}{\sqrt{10}}$ .

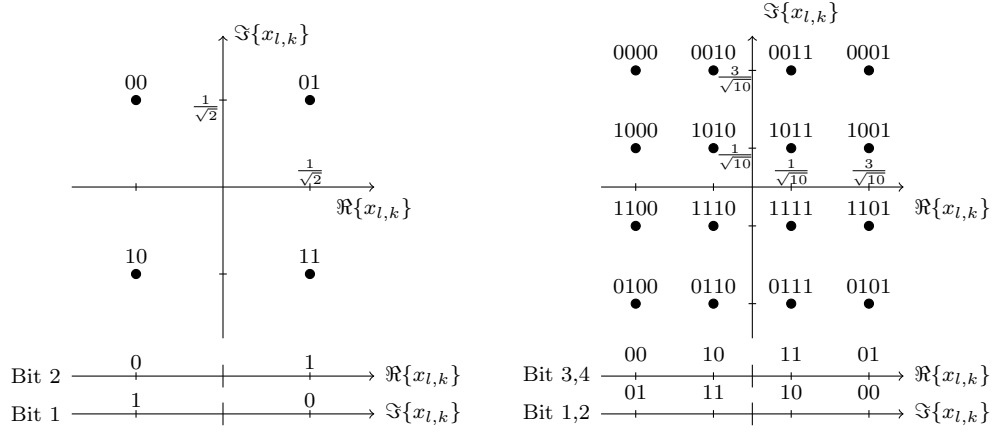


Figure 4.2: 4-QAM and 16-QAM, Gray code

#### 4.2.1. 4-QAM

For 4-QAM, the absolute value of the channel estimates does not affect the demapping so that a division by  $\hat{h}_{l,k}$  is equivalent to a multiplication with  $\hat{h}_{l,k}^*$ . Equation (4.4) can thus be written as:

$$\hat{x}_{l,k} = y_{l,k} \hat{h}_{l,k}^*. \quad (4.20)$$

Because the received symbol  $y_{l,k}$  as well as the channel estimate  $\hat{h}_{l,k}$  are Gaussian variables (conditioned on the transmitted data symbol  $x_{l,k}$ ), the BEP can be calculated by applying Lemma 1 in Equation (4.20).

At data position  $(\{l, k\} \notin \mathcal{P})$ , the required conditional correlation of  $y_{l,k}$  with  $\hat{h}_{l,k}^*$  can be found as:

$$\mathbb{E} \left\{ y_{l,k} \hat{h}_{l,k}^* \middle| x_{l,k} \right\} = \sum_{\{l_p, k_p\} \in \mathcal{P}} \sum_{d_2=1}^L \sum_{d_1=1}^L \mathbb{E} \left\{ (\mathbf{D}_k)_{l,d_1} (\mathbf{D}_{k_p})_{l_p,d_2}^* \frac{x_{d_1,k} x_{d_2,k_p}^*}{x_{l_p,k_p}^*} \right\} (\mathbf{w}_{l,k})_{\{l_p, k_p\}} \quad (4.21)$$

$$= \mathbf{R}_{h_{l,k}, \hat{\mathbf{h}}_{\mathcal{P}}^{\text{LS}}} \mathbf{w}_{l,k} x_{l,k}. \quad (4.22)$$

The mean power of the channel estimate  $\hat{h}_{l,k}$  and the received symbol  $y_{l,k}$  is given as:

$$\mathbb{E} \left\{ \hat{h}_{l,k} \hat{h}_{l,k}^* \right\} = \mathbf{w}_{l,k}^H \mathbf{R}_{\hat{\mathbf{h}}_{\mathcal{P}}^{\text{LS}}} \mathbf{w}_{l,k}, \quad (4.23)$$

$$\mathbb{E} \left\{ y_{l,k} y_{l,k}^* \middle| x_{l,k} \right\} = P_{S_{l,k}} x_{l,k} x_{l,k}^* + P_{\text{ICI}_{l,k}} + P_{\text{noise}_{l,k}}. \quad (4.24)$$

The probability that the second bit is wrongfully detected as a “0”, while a “1” was sent (see Figure 4.2), is given by the law of total probability as the average of  $\Pr\left(\Re\{y_{l,k}\hat{h}_{l,k}^*\} < 0 \middle| \frac{1+j}{\sqrt{2}}\right)$  and  $\Pr\left(\Re\{y_{l,k}\hat{h}_{l,k}^*\} < 0 \middle| \frac{1-j}{\sqrt{2}}\right)$ . Because of symmetry, this probability represents also the case for all other bit errors (they can be rotated to the above described case), so that the BEP can be written as:

$$\text{BEP}_{l,k}^{4\text{QAM}}(\mathbf{w}_{l,k}) = \frac{1}{2} \Pr\left(\Re\{y_{l,k}\hat{h}_{l,k}^*\} < 0 \middle| \frac{1+j}{\sqrt{2}}\right) + \frac{1}{2} \Pr\left(\Re\{y_{l,k}\hat{h}_{l,k}^*\} < 0 \middle| \frac{1-j}{\sqrt{2}}\right). \quad (4.25)$$

By applying Lemma 1 and including Equation (4.22) to (4.24), the BEP for 4-QAM can be simplified to:

$$\begin{aligned} \text{BEP}_{l,k}^{4\text{QAM}}(\mathbf{w}_{l,k}) = \frac{1}{2} & - \frac{\Re\{\mathbf{R}_{h_{l,k}, \hat{\mathbf{h}}_{\mathcal{P}}^{\text{LS}}}\mathbf{w}_{l,k}\} - \Im\{\mathbf{R}_{h_{l,k}, \hat{\mathbf{h}}_{\mathcal{P}}^{\text{LS}}}\mathbf{w}_{l,k}\}}{4\sqrt{2(P_{S_{l,k}} + P_{\text{ICI}_{l,k}} + P_{\text{noise}_{l,k}})}\mathbf{w}_{l,k}^H \mathbf{R}_{\hat{\mathbf{h}}_{\mathcal{P}}^{\text{LS}}}\mathbf{w}_{l,k} - \left(\Re\{\mathbf{R}_{h_{l,k}, \hat{\mathbf{h}}_{\mathcal{P}}^{\text{LS}}}\mathbf{w}_{l,k}\} + \Im\{\mathbf{R}_{h_{l,k}, \hat{\mathbf{h}}_{\mathcal{P}}^{\text{LS}}}\mathbf{w}_{l,k}\}\right)^2} \\ & - \frac{\Re\{\mathbf{R}_{h_{l,k}, \hat{\mathbf{h}}_{\mathcal{P}}^{\text{LS}}}\mathbf{w}_{l,k}\} + \Im\{\mathbf{R}_{h_{l,k}, \hat{\mathbf{h}}_{\mathcal{P}}^{\text{LS}}}\mathbf{w}_{l,k}\}}{4\sqrt{2(P_{S_{l,k}} + P_{\text{ICI}_{l,k}} + P_{\text{noise}_{l,k}})}\mathbf{w}_{l,k}^H \mathbf{R}_{\hat{\mathbf{h}}_{\mathcal{P}}^{\text{LS}}}\mathbf{w}_{l,k} - \left(\Re\{\mathbf{R}_{h_{l,k}, \hat{\mathbf{h}}_{\mathcal{P}}^{\text{LS}}}\mathbf{w}_{l,k}\} - \Im\{\mathbf{R}_{h_{l,k}, \hat{\mathbf{h}}_{\mathcal{P}}^{\text{LS}}}\mathbf{w}_{l,k}\}\right)^2}. \end{aligned} \quad (4.26)$$

Clearly, the interpolation vector  $\mathbf{w}_{l,k}$  has to compensate average phase shifts in order to minimize the BEP. This condition implies that the imaginary part of the scalar  $\mathbf{R}_{h_{l,k}, \hat{\mathbf{h}}_{\mathcal{P}}^{\text{LS}}}\mathbf{w}_{l,k}$  has to be zero. The real part on the other hand has to be larger than zero so that the interpolation becomes better than a random guess. I therefore define a new BEP (tilde) in which I assume that  $\Re\{\mathbf{R}_{h_{l,k}, \hat{\mathbf{h}}_{\mathcal{P}}^{\text{LS}}}\mathbf{w}_{l,k}\} > 0$  and  $\Im\{\mathbf{R}_{h_{l,k}, \hat{\mathbf{h}}_{\mathcal{P}}^{\text{LS}}}\mathbf{w}_{l,k}\} = 0$ . Equation (4.26) then simplifies to:

$$\widetilde{\text{BEP}}_{l,k}^{4\text{QAM}}(\mathbf{w}_{l,k}) = \frac{1}{2} - \frac{1}{2\sqrt{2(P_{S_{l,k}} + P_{\text{ICI}_{l,k}} + P_{\text{noise}_{l,k}})}\frac{\mathbf{w}_{l,k}^H \mathbf{R}_{\hat{\mathbf{h}}_{\mathcal{P}}^{\text{LS}}}\mathbf{w}_{l,k}}{(\mathbf{R}_{h_{l,k}, \hat{\mathbf{h}}_{\mathcal{P}}^{\text{LS}}}\mathbf{w}_{l,k})^2} - 1}. \quad (4.27)$$

In order to minimize Equation 4.27, the generalized Rayleigh quotient[21] inside the square root has to be minimized, or equivalently, the inverse quotient

maximized:

$$\arg \min_{\mathbf{w}_{l,k}^H} \widetilde{\text{BEP}}_{l,k}^{4\text{QAM}}(\mathbf{w}_{l,k}^H) = \arg \min_{\mathbf{w}_{l,k}^H} \left( \frac{\mathbf{w}_{l,k}^H \mathbf{R}_{\hat{\mathbf{h}}_{\mathcal{P}}^{\text{LS}}} \mathbf{w}_{l,k}}{(\mathbf{R}_{h_{l,k}, \hat{\mathbf{h}}_{\mathcal{P}}^{\text{LS}}} \mathbf{w}_{l,k})^2} \right) \quad (4.28)$$

$$= \arg \max_{\mathbf{w}_{l,k}^H} \left( \frac{\mathbf{w}_{l,k}^H \mathbf{R}_{h_{l,k}, \hat{\mathbf{h}}_{\mathcal{P}}^{\text{LS}}}^H \mathbf{R}_{h_{l,k}, \hat{\mathbf{h}}_{\mathcal{P}}^{\text{LS}}} \mathbf{w}_{l,k}}{\mathbf{w}_{l,k}^H \mathbf{R}_{\hat{\mathbf{h}}_{\mathcal{P}}^{\text{LS}}} \mathbf{w}_{l,k}} \right) \quad (4.29)$$

Because the matrices in the nominator and denominator are positive-definite, the maximization in Equation (4.29) becomes a generalized eigenvalue problem:

$$\mathbf{R}_{h_{l,k}, \hat{\mathbf{h}}_{\mathcal{P}}^{\text{LS}}}^H \mathbf{R}_{h_{l,k}, \hat{\mathbf{h}}_{\mathcal{P}}^{\text{LS}}} \mathbf{w}_{l,k} = \lambda \mathbf{R}_{\hat{\mathbf{h}}_{\mathcal{P}}^{\text{LS}}} \mathbf{w}_{l,k}. \quad (4.30)$$

The unique solution for Equation (4.30) can be found by inserting the MMSE estimation as:

$$\mathbf{R}_{h_{l,k}, \hat{\mathbf{h}}_{\mathcal{P}}^{\text{LS}}}^H \underbrace{\mathbf{R}_{h_{l,k}, \hat{\mathbf{h}}_{\mathcal{P}}^{\text{LS}}} \mathbf{R}_{\hat{\mathbf{h}}_{\mathcal{P}}^{\text{LS}}} \mathbf{R}_{h_{l,k}, \hat{\mathbf{h}}_{\mathcal{P}}^{\text{LS}}}^H}_{\lambda} = \lambda \mathbf{R}_{h_{l,k}, \hat{\mathbf{h}}_{\mathcal{P}}^{\text{LS}}}^H. \quad (4.31)$$

Thus, the MMSE estimation also minimizes the BEP.

$$(\mathbf{w}_{l,k}^H)^{4\text{QAM}, \text{minBEP}} = \arg \min_{\mathbf{w}_{l,k}^H} \text{BEP}_{l,k}^{4\text{QAM}}(\mathbf{w}_{l,k}^H) = \mathbf{R}_{h_{l,k}, \hat{\mathbf{h}}_{\mathcal{P}}^{\text{LS}}} \mathbf{R}_{\hat{\mathbf{h}}_{\mathcal{P}}^{\text{LS}}}^{-1}. \quad (4.32)$$

Because the MSE has to be larger than zero, Equation (4.10) delivers the following inequality for  $(\mathbf{w}_{l,k}^H)^{4\text{QAM}, \text{minBEP}}$ :

$$P_{S_{l,k}} \geq \mathbf{R}_{h_{l,k}, \hat{\mathbf{h}}_{\mathcal{P}}^{\text{LS}}} \mathbf{R}_{\hat{\mathbf{h}}_{\mathcal{P}}^{\text{LS}}}^{-1} \mathbf{R}_{h_{l,k}, \hat{\mathbf{h}}_{\mathcal{P}}^{\text{LS}}}^H. \quad (4.33)$$

Inserting the minimum value of the Rayleigh quotient  $(1/\lambda)$  in Equation (4.27) and applying the Inequality (4.33), it follows immediately that:

$$0 \leq \widetilde{\text{BEP}}_{l,k}^{4\text{QAM}}(\mathbf{w}_{l,k}) \leq 1/2 \quad (4.34)$$

Not that this BEP is upper bounded by 1/2 due to the assumption of  $\Re\{\mathbf{R}_{h_{l,k}, \hat{\mathbf{h}}_{\mathcal{P}}^{\text{LS}}} \mathbf{w}_{l,k}\} > 0$ .

Equation (4.27) can also be used to calculate the BEP for perfect channel knowledge (Equation (4.3)) by inserting the MMSE interpolation and setting

the MSE to zero (Equation (4.10)), which leads to:

$$\text{BEP}_{l,k}^{4\text{QAM,perfect}} = \frac{1}{2} - \frac{1}{2\sqrt{1 + 2\frac{P_{\text{CI},l,k} + P_{\text{noise},l,k}}{P_{\text{S},l,k}}}}}. \quad (4.35)$$

#### 4.2.2. 16-QAM

I now calculate the BEP for 16-QAM. For the second and fourth bit it can be found very similar to the case of 4-QAM (see Figure 4.2):

$$\text{BEP}_{l,k}^{16\text{QAM,Bit2\&4}}(\mathbf{w}_{l,k}) = \frac{1}{8} \sum_{\substack{q_r \in \\ \{1,3\}}} \sum_{\substack{q_i \in \{-3, \\ -1,1,3\}}} \Pr\left(\Re\{y_{l,k} \hat{h}_{l,k}^*\} < 0 \middle| \frac{q_r + jq_i}{\sqrt{10}}\right). \quad (4.36)$$

Equation (C.1) gives the result of applying Lemma 1 to (4.36) and Equation (C.2) provides an expression for the case of  $\Re\{\mathbf{R}_{h_{l,k}, \hat{\mathbf{h}}_{\mathcal{P}}^{\text{LS}}} \mathbf{w}_{l,k}\} > 0$  and  $\Im\{\mathbf{R}_{h_{l,k}, \hat{\mathbf{h}}_{\mathcal{P}}^{\text{LS}}} \mathbf{w}_{l,k}\} = 0$ . Similar to 4-QAM, the MMSE interpolation also minimizes the BEP for 16-QAM (bit 2 and 4).

The BEP for the first and third bit has a different structure compared to the second and fourth. Figure 4.2 shows that the decision region is limited between  $-\frac{2}{\sqrt{10}}$  and  $\frac{2}{\sqrt{10}}$ , so that the BEP conditioned on a “1” is no longer equal to that of a “0”. The unconditional BEP can then be found as:

$$\begin{aligned} \text{BEP}_{l,k}^{16\text{QAM,Bit1\&3}}(\mathbf{w}_{l,k}) = & \frac{1}{8} \sum_{\substack{q_i \in \{-3, \\ -1,1,3\}}} \left( 1 - \left[ \Pr\left(\Re\left\{\frac{y_{l,k}}{\hat{h}_{l,k}}\right\} < \frac{2}{\sqrt{10}} \middle| \frac{1+jq_i}{\sqrt{10}}\right) - \Pr\left(\Re\left\{\frac{y_{l,k}}{\hat{h}_{l,k}}\right\} < \frac{-2}{\sqrt{10}} \middle| \frac{1+jq_i}{\sqrt{10}}\right) \right] \right) \\ & + \frac{1}{8} \sum_{\substack{q_i \in \{-3, \\ -1,1,3\}}} \left[ \Pr\left(\Re\left\{\frac{y_{l,k}}{\hat{h}_{l,k}}\right\} < \frac{2}{\sqrt{10}} \middle| \frac{3+jq_i}{\sqrt{10}}\right) - \Pr\left(\Re\left\{\frac{y_{l,k}}{\hat{h}_{l,k}}\right\} < \frac{-2}{\sqrt{10}} \middle| \frac{3+jq_i}{\sqrt{10}}\right) \right] \end{aligned} \quad (4.37)$$

Lemma 1 can no longer be applied directly in Equation (4.37) but the probabilities  $\Pr(\cdot)$  can be rewritten:

$$\Pr\left(\Re\left\{\frac{y_{l,k}}{\hat{h}_{l,k}}\right\} < a \middle| x_{l,k}\right) = \Pr\left(\Re\left\{y_{l,k} \hat{h}_{l,k}^*\right\} < a \hat{h}_{l,k} \hat{h}_{l,k}^* \middle| x_{l,k}\right) \quad (4.38)$$

$$= \Pr\left(\Re\left\{(y_{l,k} - a \hat{h}_{l,k}) \hat{h}_{l,k}^*\right\} < 0 \middle| x_{l,k}\right), \quad (4.39)$$

so that Lemma 1 can again be used. The required conditional correlation and mean power can be calculated as:

$$\mathbb{E} \left\{ \left( y_{l,k} - a \hat{h}_{l,k} \right) \left( y_{l,k} - a \hat{h}_{l,k} \right)^* \middle| x_{l,k} \right\} = P_{S_{l,k}} x_{l,k} x_{l,k}^* + P_{\text{ICI}_{l,k}} + P_{\text{noise}_{l,k}} - 2a \Re \left\{ \mathbf{R}_{h_{l,k}, \hat{\mathbf{h}}_{\mathcal{P}}^{\text{LS}}} \mathbf{w}_{l,k} x_{l,k} \right\} + a^2 \mathbf{w}_{l,k}^H \mathbf{R}_{\hat{\mathbf{h}}_{\mathcal{P}}^{\text{LS}}} \mathbf{w}_{l,k}, \quad (4.40)$$

$$\mathbb{E} \left\{ \left( y_{l,k} - a \hat{h}_{l,k} \right) \hat{h}_{l,k}^* \middle| x_{l,k} \right\} = \mathbf{R}_{h_{l,k}, \hat{\mathbf{h}}_{\mathcal{P}}^{\text{LS}}} \mathbf{w}_{l,k} x_{l,k} - a \mathbf{w}_{l,k}^H \mathbf{R}_{\hat{\mathbf{h}}_{\mathcal{P}}^{\text{LS}}} \mathbf{w}_{l,k}. \quad (4.41)$$

Applying Lemma 1 and including Equation (4.41) and (4.40) into (4.38), gives a closed form solution for the probability  $\Pr \left( \Re \left\{ \frac{y_{l,k}}{\hat{h}_{l,k}} \right\} < a \middle| x_{l,k} \right)$  and can be found in Appendix C (Equation (C.3)).

Finally, the overall BEP can be obtained as:

$$\text{BEP}_{l,k}^{16\text{QAM}}(\mathbf{w}_{l,k}) = \frac{1}{2} \left( \text{BEP}_{l,k}^{16\text{QAM}, \text{Bit1\&3}}(\mathbf{w}_{l,k}) + \text{BEP}_{l,k}^{16\text{QAM}, \text{Bit2\&4}}(\mathbf{w}_{l,k}) \right). \quad (4.42)$$

Note that Equation (4.36), (4.37) and (C.3) can be used in order to get a numerical result of the BEP (Equation (4.42)).

Examining Equation (4.42), one can naturally ask what interpolation method minimizes the BEP. Numerical evaluations suggest that a scaled MMSE interpolation performs this task<sup>2</sup>. This result is, to some extent, intuitive: the MMSE interpolation minimizes the BEP for the second and fourth bit which is, in contrast to the BEP of the first and third bit, independent of a scaling factor. Therefore the factor can be chosen so that the BEP of the first and third bit is minimized. The interpolation method that minimizes the BEP for 16-QAM can thus be written as:

$$(\mathbf{w}_{l,k}^H)^{16\text{QAM}, \text{minBEP}} = \arg \min_{\mathbf{w}_{l,k}^H} \text{BEP}_{l,k}^{16\text{QAM}}(\mathbf{w}_{l,k}^H) = \alpha_{l,k} \mathbf{R}_{h_{l,k}, \hat{\mathbf{h}}_{\mathcal{P}}^{\text{LS}}} \mathbf{R}_{\hat{\mathbf{h}}_{\mathcal{P}}^{\text{LS}}}^{-1}, \quad (4.43)$$

where the real valued scaling factor  $\alpha_{l,k}$  can be found numerically.

Figure 4.3 gives a numerical example for the case of 73 subcarriers, 5 OFDM symbols, 146 samples, a Jakes Doppler spectrum ( $\nu_{\max} T_s = 0.002$ ), a uniform power delay profile ( $\tau_{\max} \Delta f = 1$ ), and a rectangular pilot grid (time

<sup>2</sup> a formal proof is beyond the scope of this thesis

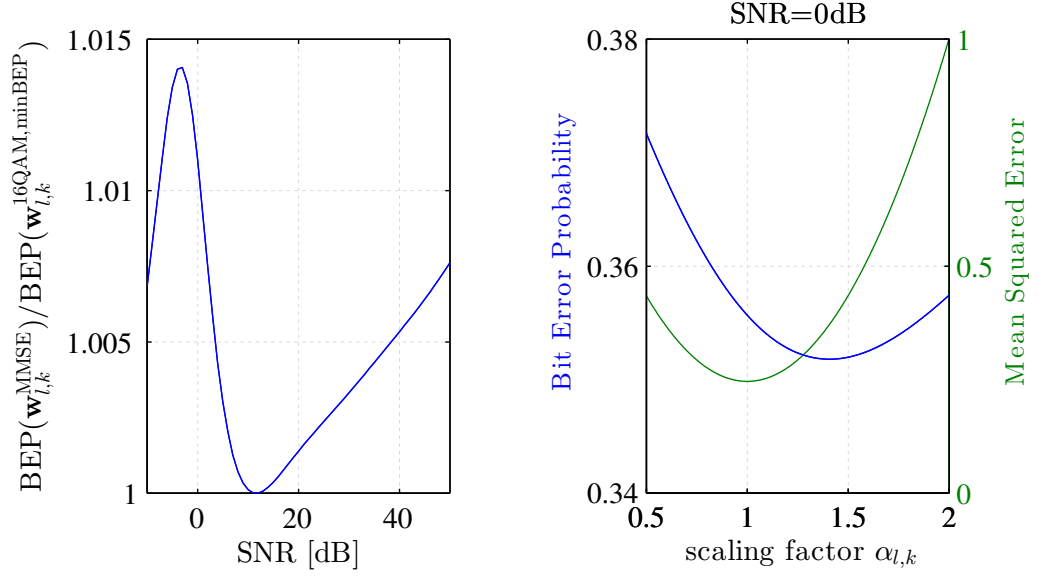


Figure 4.3: MMSE vs. Minimum BEP Interpolation for 16-QAM, potential improvement by scaling factor is low

frequency spacing of 4 respectively 6). The left figure shows the BEP<sup>3</sup> of the MMSE interpolation  $(\mathbf{w}_{l,k}^H)^{\text{MMSE}}$  relative to the BEP of the minimum BEP interpolation  $(\mathbf{w}_{l,k}^H)^{\text{16QAM,minBEP}}$ . This ratio is usually below 1% so that potential improvements by using  $(\mathbf{w}_{l,k}^H)^{\text{16QAM,minBEP}}$  are small. Also, there exists a Signal-to-Noise Ratio (SNR) where both interpolation methods are equal. The right figure gives the BEP as well as the MSE as a function of the scaling factor  $\alpha_{l,k}$ <sup>4</sup>. A factor one minimizes the MSE while a scaling of two results in an MSE equal to the signal power ( $\text{MSE}_{l,k}(2(\mathbf{w}_{l,k}^H)^{\text{MMSE}}) = P_{S_{l,k}}$ ). For low SNR, the optimal scaling is larger than one while for large ratios it has to be smaller.

Similar to the case of 4-QAM, Equation (4.42) can also be used to calculate the BEP for perfect channel knowledge. By assuming a MMSE interpolation and a MSE of zero, Equation (C.3) becomes:

$$\Pr \left( \Re \left\{ \frac{y_{l,k}}{h_{l,k}} \right\} < \frac{a}{\sqrt{10}} \left| \frac{q_r + jq_i}{\sqrt{10}} \right| \right) = \frac{1}{2} - \frac{q_r - a}{2\sqrt{(q_r - a)^2 + 10 \frac{(P_{\text{ICI}_{l,k}} + P_{\text{noise}_{l,k}})}{P_{S_{l,k}}}}}, \quad (4.44)$$

<sup>3</sup> averaged over all data positions

<sup>4</sup> assumed to be constant over all positions

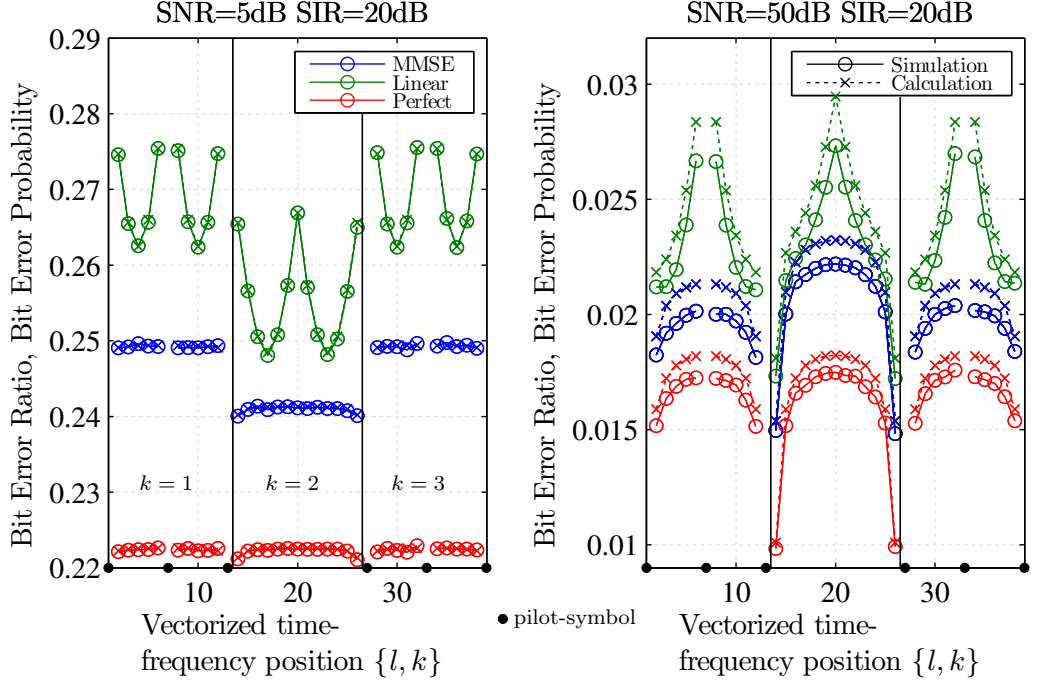


Figure 4.4: BER vs. BEP as a function of the time-frequency position, influence of interpolation, simulation and calculation coincide (left), simulation and calculation differ due to non-Gaussian ICI (right)

and, by inserting this probability in (4.36) and (4.37), leads to the BEP for a perfectly known channel:

$$\text{BEP}_{l,k}^{16\text{QAM,perfect}} = \frac{1}{2} - \frac{3}{8\sqrt{1 + 10\frac{(P_{\text{ICI}_{l,k}} + P_{\text{noise}_{l,k}})}{P_{\text{S}_{l,k}}}}} - \frac{6}{8\sqrt{9 + 10\frac{(P_{\text{ICI}_{l,k}} + P_{\text{noise}_{l,k}})}{P_{\text{S}_{l,k}}}}} + \frac{5}{8\sqrt{25 + 10\frac{(P_{\text{ICI}_{l,k}} + P_{\text{noise}_{l,k}})}{P_{\text{S}_{l,k}}}}} \quad (4.45)$$

#### 4.2.3. Simulations

As already derived in Chapter 3, the ICI is not Gaussian distributed so that the calculated BEP (Equation (4.26) and (4.42)) represents only an approximation if the ICI power is larger than the noise power. I thus compare the calculated BEP with simulations (1 million realization), whereas for the latter, Equation (2.10) and (2.24) are used. For the numerical example I assume 16-QAM, 13 subcarriers, 3 OFDM symbols, 26 samples, flat fading, and a rectangular pilot

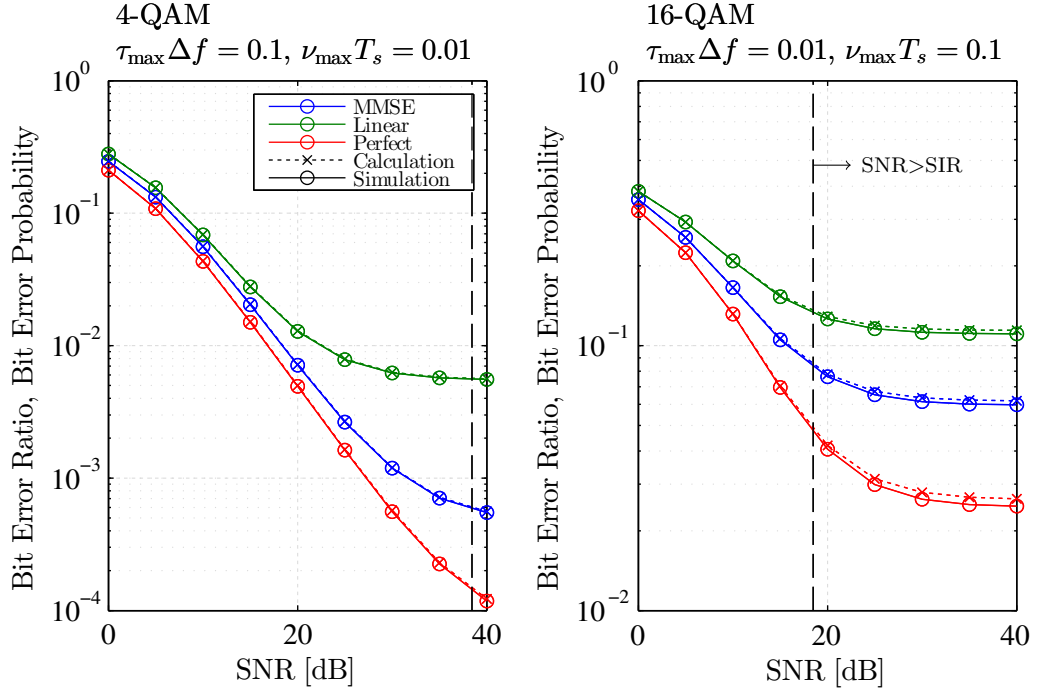


Figure 4.5: BER vs. BEP as a function of SNR, influence of interpolation, simulations and calculations coincide for  $\text{SNR} < \text{SIR}$

grid (time-, frequency-spacing of 2 respectively 6). Furthermore I assume a Jakes Doppler spectrum ( $\nu_{\max}T_s = 0.08$ ) which gives a SIR of 20 dB. The left part of Figure 4.4 shows that simulation and calculation coincides since the noise power is larger then the ICI power. Note also, that linear interpolation act as a smoother which explains why the BEP between two pilot-symbols is better then the BEP near one of them. In the right figure on the other hand the simulation differs from the calculation but the principal shapes are similar. So even if the calculation overestimates the BEP, comparing different interpolation methods still gives reasonable results.

Figure 4.5 gives another example for 19 subcarriers, 13 OFDM symbols and a rectangular pilot grid (time-, frequency-spacing of 4 respectively 6). In contrast to Figure 4.4, the BER is averaged over time and frequency, and plotted as a function of the SNR. Again, simulations confirm the analytical BEP expression if the noise power is larger than the ICI-power. However, even for higher ICI-power, the error of the closed-form solution remains relatively low (smaller than 3%).

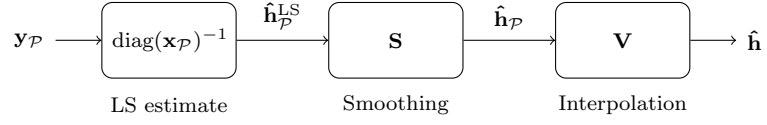


Figure 4.6: Separated Smoothing and Interpolation,

### 4.3. Interpolation

At the beginning of this Section I will state some general properties of the investigated interpolation methods while the next Subsections provide a closer look at specific methods.

As explained at the beginning of this Chapter, the channel estimate  $\hat{h}_{l,k}$  can be obtained as:

$$\hat{h}_{l,k} = \mathbf{w}_{l,k}^H \hat{\mathbf{h}}_{\mathcal{P}}^{\text{LS}}, \quad (4.46)$$

where  $\mathbf{w}_{l,k}$  represents the interpolation vector. Equation (4.46) shows immediately that such a channel estimation is linear in the following sense:

$$\hat{h}_{l,k} = \mathbf{w}_{l,k}^H \left( a \hat{\mathbf{h}}_{1,\mathcal{P}}^{\text{LS}} + b \hat{\mathbf{h}}_{2,\mathcal{P}}^{\text{LS}} \right) = a \mathbf{w}_{l,k}^H \hat{\mathbf{h}}_{1,\mathcal{P}}^{\text{LS}} + b \mathbf{w}_{l,k}^H \hat{\mathbf{h}}_{2,\mathcal{P}}^{\text{LS}}, \quad (4.47)$$

where  $a$  and  $b$  are some arbitrary scalars. Linearity allows the separation of the weighting vector  $\mathbf{w}_{l,k}$  into a smoothing- and an interpolation part (see Figure 4.6), as suggested in [22]. The smoothing part filters out noise at pilot positions only while the interpolation part can be designed to be independent of noise. Such a separation provides the opportunity to identify whether some improvements are caused by interpolation or by more accurate estimates at pilot positions. The vectorized channel estimate can then be written as

$$\hat{\mathbf{h}} = \mathbf{V} \mathbf{S} \hat{\mathbf{h}}_{\mathcal{P}}^{\text{LS}}, \quad (4.48)$$

whereby  $\mathbf{S}$  describes the smoothing and  $\mathbf{V}$  the interpolation matrix. Linearity also simplifies finding the matrix  $V$  because it can be interpreted as a shift-variant “impulse response”: The  $i$ -th column vector of the matrix  $V$  can be found by applying the interpolation method to a vector that consist mainly of zeros except the  $i$ -th position, which is a one.

Figure 4.7 shows the pilot patterns I use for numerical evaluation. The pilot spacing in the time domain  $\Delta p_t$  and in the frequency domain  $\Delta p_f$  are chosen

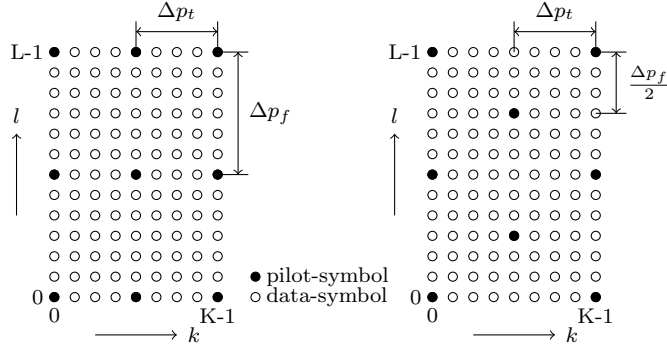


Figure 4.7: Rectangular- and diamond-shaped pilot pattern

Number of subcarriers	145
Number of OFDM symbols	49
Number of samples	290
frequency pilot spacing	6
time pilot spacing	4
power delay profile	uniform
Doppler spectral density	Jakes
“high doubly-selective”	$\tau_{\max}\Delta f = 0.1, \nu_{\max}T_s = 0.055$
“low doubly-selective”	$\tau_{\max}\Delta f = 0.029, \nu_{\max}T_s = 0.016$

Table 4.1.: Parameter used for evaluation of different interpolation methods

similar to the LTE standard<sup>5</sup> i.e.,  $\Delta p_t = 4$  and  $\Delta p_f = 6$ .

As already mentioned in Section 2.1, I assume a Jakes Doppler spectrum and a uniform power delay profile. The channel parameters are chosen so that the autocorrelation function between two pilot-symbols is 0.5 for a “high doubly-selective” channel ( $\tau_{\max}\Delta f = 0.1, \nu_{\max}T_s = 0.055 \Rightarrow \text{SIR}=23 \text{ dB}$ ) and 0.95 for a “low doubly-selective” channel ( $\tau_{\max}\Delta f = 0.029, \nu_{\max}T_s = 0.016 \Rightarrow \text{SIR}=34 \text{ dB}$ ). Furthermore I assume 145 subcarriers, 49 OFDM symbols and 290 samples.

Table 4.1 summarizes the parameters, used for numerical evaluation of different interpolation methods. In order to calculate the BEP, Equation (4.26) and Equation (4.42) can be applied. I further compare each interpolation method for no-smoothing (LS) and MMSE-smoothing (Equation 4.50).

<sup>5</sup> LTE uses only a diamond shaped pattern and  $\Delta p_t$  alternates between 3 and 4

### 4.3.1. Optimal Interpolation

The optimal interpolation was already derived in Section 4.2.1 and 4.2.2, where it was found that the MMSE channel estimation also minimizes the BEP. The optimal smoothing and interpolation matrix can thus be written as:

$$(\mathbf{w}^{\text{LMMSE}})^H = \mathbf{R}_{\mathbf{h}, \mathbf{h}_{\mathcal{P}}} (\mathbf{R}_{\mathbf{h}_{\mathcal{P}}} + \text{diag}(\mathbf{p}_{\text{ICI}_{\mathcal{P}}} + \mathbf{p}_{\text{noise}_{\mathcal{P}}}))^{-1} \quad (4.49)$$

$$= \underbrace{\mathbf{R}_{\mathbf{h}, \mathbf{h}_{\mathcal{P}}} \mathbf{R}_{\mathbf{h}_{\mathcal{P}}}^{-1}}_{\mathbf{V}^{\text{LMMSE}}} \underbrace{\mathbf{R}_{\mathbf{h}_{\mathcal{P}}} (\mathbf{R}_{\mathbf{h}_{\mathcal{P}}} + \text{diag}(\mathbf{p}_{\text{ICI}_{\mathcal{P}}} + \mathbf{p}_{\text{noise}_{\mathcal{P}}}))^{-1}}_{\mathbf{S}^{\text{LMMSE}}}. \quad (4.50)$$

Equation (4.50) shows that the optimal channel estimation can be obtained as a noise-independent interpolation of the MMSE channel estimates at pilot positions:

$$\hat{\mathbf{h}}^{\text{LMMSE}} = \mathbf{V}^{\text{LMMSE}} \hat{\mathbf{h}}_{\mathcal{P}}^{\text{LMMSE}} \quad (4.51)$$

For the special case of

- WSSUS,
- rectangular-shaped pilot-symbol pattern, and
- separable time-frequency correlation,

I will show that the optimal 2D interpolation  $\mathbf{V}^{\text{LMMSE}}$  is equivalent to successively applying two independent one-Dimensional (1D) interpolations. The correlation matrix  $\mathbf{R}_{\mathbf{h}_{\mathcal{P}}}$  and the cross-correlation matrix  $\mathbf{R}_{\mathbf{h}, \mathbf{h}_{\mathcal{P}}}$  can be obtained as the Kronecker product of the corresponding “1D” correlation matrices:

$$\mathbf{R}_{\mathbf{h}_{\mathcal{P}}} = \mathbf{R}_{\mathbf{h}_{\mathcal{P}_t}} \otimes \mathbf{R}_{\mathbf{h}_{\mathcal{P}_f}} \quad (4.52)$$

$$\mathbf{R}_{\mathbf{h}, \mathbf{h}_{\mathcal{P}}} = \mathbf{R}_{\mathbf{h}_t, \mathbf{h}_{\mathcal{P}_t}} \otimes \mathbf{R}_{\mathbf{h}_f, \mathbf{h}_{\mathcal{P}_f}}, \quad (4.53)$$

so that the optimal interpolation  $\mathbf{V}^{\text{LMMSE}}$  can also be written as the Kronecker product of “1D” interpolation matrices  $\mathbf{V}_t^{\text{LMMSE}}$  and  $\mathbf{V}_f^{\text{LMMSE}}$ :

$$\mathbf{V}^{\text{LMMSE}} = \left( \mathbf{R}_{\mathbf{h}_t, \mathbf{h}_{\mathcal{P}_t}} \otimes \mathbf{R}_{\mathbf{h}_f, \mathbf{h}_{\mathcal{P}_f}} \right) \left( \mathbf{R}_{\mathbf{h}_{\mathcal{P}_t}} \otimes \mathbf{R}_{\mathbf{h}_{\mathcal{P}_f}} \right)^{-1} \quad (4.54)$$

$$= \underbrace{\mathbf{R}_{\mathbf{h}_t, \mathbf{h}_{\mathcal{P}_t}} (\mathbf{R}_{\mathbf{h}_{\mathcal{P}_t}})^{-1}}_{\mathbf{V}_t^{\text{LMMSE}}} \otimes \underbrace{\mathbf{R}_{\mathbf{h}_f, \mathbf{h}_{\mathcal{P}_f}} (\mathbf{R}_{\mathbf{h}_{\mathcal{P}_f}})^{-1}}_{\mathbf{V}_f^{\text{LMMSE}}}. \quad (4.55)$$

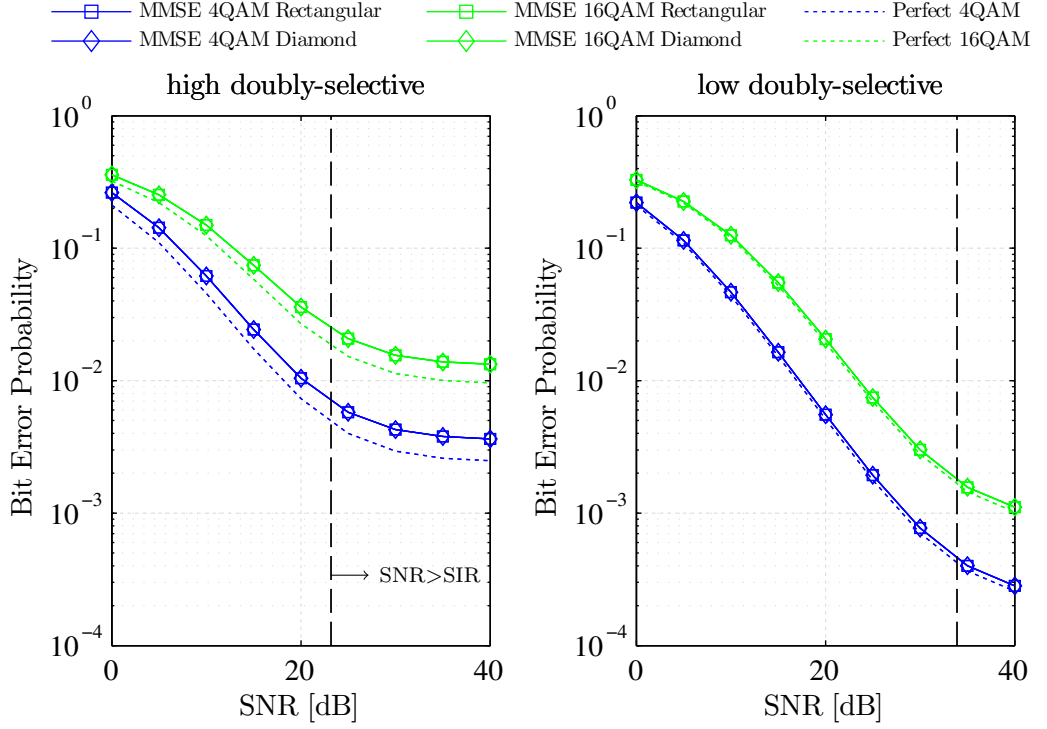


Figure 4.8: Optimal Interpolation, BEP as a function of SNR, influence of MMSE interpolation, pilot-symbol pattern and modulation order

Finally, inserting Equation (4.55) in (4.51) gives:

$$\hat{\mathbf{h}}^{\text{LMMSE}} = \mathbf{V}^{\text{LMMSE}} \hat{\mathbf{h}}_{\mathcal{P}}^{\text{LMMSE}} \quad (4.56)$$

$$= (\mathbf{V}_t^{\text{LMMSE}} \otimes \mathbf{V}_f^{\text{LMMSE}}) \text{vec} \left\{ \hat{\mathbf{H}}_{\mathcal{P}}^{\text{LMMSE}} \right\} \quad (4.57)$$

$$= \text{vec} \left\{ \mathbf{V}_f^{\text{LMMSE}} \hat{\mathbf{H}}_{\mathcal{P}}^{\text{LMMSE}} (\mathbf{V}_t^{\text{LMMSE}})^T \right\}, \quad (4.58)$$

where  $\hat{\mathbf{H}}_{\mathcal{P}}^{\text{LMMSE}}$  represents the  $|\mathcal{P}_f| \times |\mathcal{P}_t|$  matrix of the MMSE estimates at pilot position. Equation (4.58) performs interpolation first in one direction, and then again in the other direction which turns out to be equivalent to the 2D interpolation. Note however, that this is only true for the interpolation- and not the smoothing-part.

Whether some interpolation methods (e.g., linear, spline) are optimal depends only on the correlation matrices. Even linear interpolation can be optimal. For that, as a necessary condition, the correlation function must exhibit a triangular shape.

Figure 4.8 compares the optimal interpolation with perfect channel knowl-

edge. The rectangular-shaped pilot pattern exhibits a lower SNR-threshold for a pure interpolation error (the SNR value where lowering the ICI-plus-noise power does not reduce the BEP) compared to a diamonded-shape pilot pattern. However, for the parameters given in Table 4.1, the Signal-to-Interference-plus-Noise Ratio (SINR) is relatively low so that the BEP for rectangular- and diamond-shaped pilot pattern are almost equal. For the “low doubly-selective” channel, the MMSE interpolation comes very close to perfect channel knowledge (BEP of MMSE is approximately 7 % higher). The SIR limits the BEP performance whereas for a “high doubly-selective” channel, this happens already at a SNR of 23 dB.

#### 4.3.2. Linear Interpolation

The 1D linear<sup>6</sup> interpolation can be found as a weighted average of two points whereas the weights are given by the distance to each point. As shown in Section 4.3.1, under certain conditions, the optimal 2D interpolation can be performed by successively 1D interpolations. This fact motivates the use of bilinear interpolation, i.e., linear interpolation first in the frequency-domain, and then in the time-domain. Note that for a rectangular-shaped pilot-symbol pattern, the order of interpolation does not matter.

Another possible 2D linear interpolation was described in [23] and is based on the Delaunay triangulation<sup>7</sup>: a plane that is spanned by the three closest pilot-symbols, is sampled at data-symbol position.

Figure 4.10 shows how the BEP of these two linear interpolation methods perform relative to the MMSE interpolation (its concrete values are given in Figure 4.8). Clearly, the MMSE interpolation represents the optimal solution, so that every point in the figure has to be larger than one. For diamond-shaped pilot-symbol pattern, two successively 1D linear interpolations perform slightly better than triangle based 2D linear interpolation. The latter is especially bad for rectangular-shaped pilot-symbol pattern.

---

<sup>6</sup> in the sense of a straight line

<sup>7</sup> see Section 4.3.4

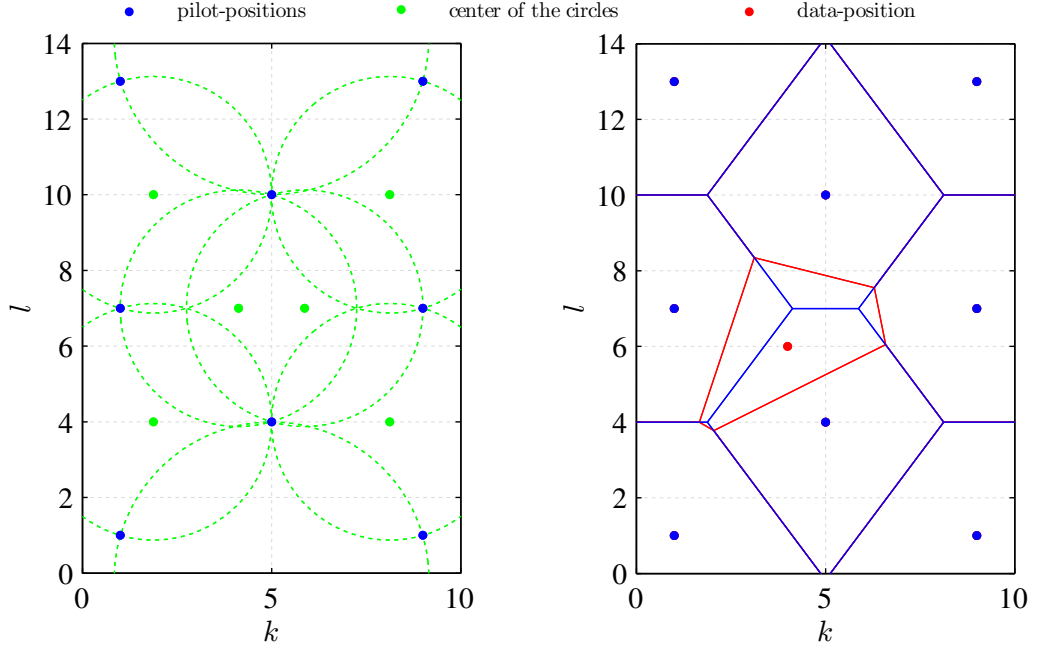


Figure 4.9: Natural Neighbor Interpolation: Voronoi diagram is based on Delaunay triangulation, weights are determined by the “stolen” area of the Voronoi diagram

#### 4.3.3. Spline Interpolation

Splines are, in general, piecewise polynomials with pieces that are smoothly connected together. However, in this thesis, only cubic splines are considered because of their minimum curvature property [24]. Similar to Section 4.3.2, spline interpolation is first performed in the frequency-domain, and then in the time-domain whereas I utilize the MATLAB built-in spline function. Note that MATLAB uses other boundary condition compared to “natural splines” [25].

For MMSE smoothing, Figure 4.11 shows that spline interpolation outperforms 1D-1D linear interpolation and, in particular, for a “low doubly-selective” channel, spline performs as good as optimal interpolation. If no smoother is used, spline also outperform linear interpolation for a “high doubly-selective” channel and high SNR, while for a “low doubly-selective” channel it performs worse. Furthermore, there is almost no difference between rectangular- and diamond-shaped pilot-symbol pattern.

#### 4.3.4. Natural Neighbor Interpolation

The natural neighbor interpolation [26] operates in two dimensions and is based on Voronoi diagrams. The left part of Figure 4.9 shows how such a diagram can be constructed: three points (pilots-positions) are connected by a circle so that no other point is inside this circle (Delaunay triangulation). Connecting the center of these circles then gives the Voronoi diagram. The right part of Figure 4.9 illustrates how this Voronoi tessellation can be used to obtain the interpolation weights: First, the Voronoi diagram of the pilot-position set is constructed and serves as a reference (blue). Second, a data-position is added and the Voronoi diagram of this new set is again created (red). The weights for the interpolation vector are then determined by the area that is “stolen” from this new Voronoi diagram.

Figure 4.12 shows the performance of natural neighbor interpolation. For “high doubly-selective” channels, successively 1D-1D linear interpolation performs slightly better than natural neighbor interpolation. This is also true for a “low doubly-selective” channel and MMSE smoothing, while in the absence of smoothing, natural neighbor interpolation delivers better results. Note also that rectangular-shaped pilot-symbol pattern outperforms diamond-shaped pilot-symbol pattern, except for MMSE smoothing in a “low doubly-selective” channel.

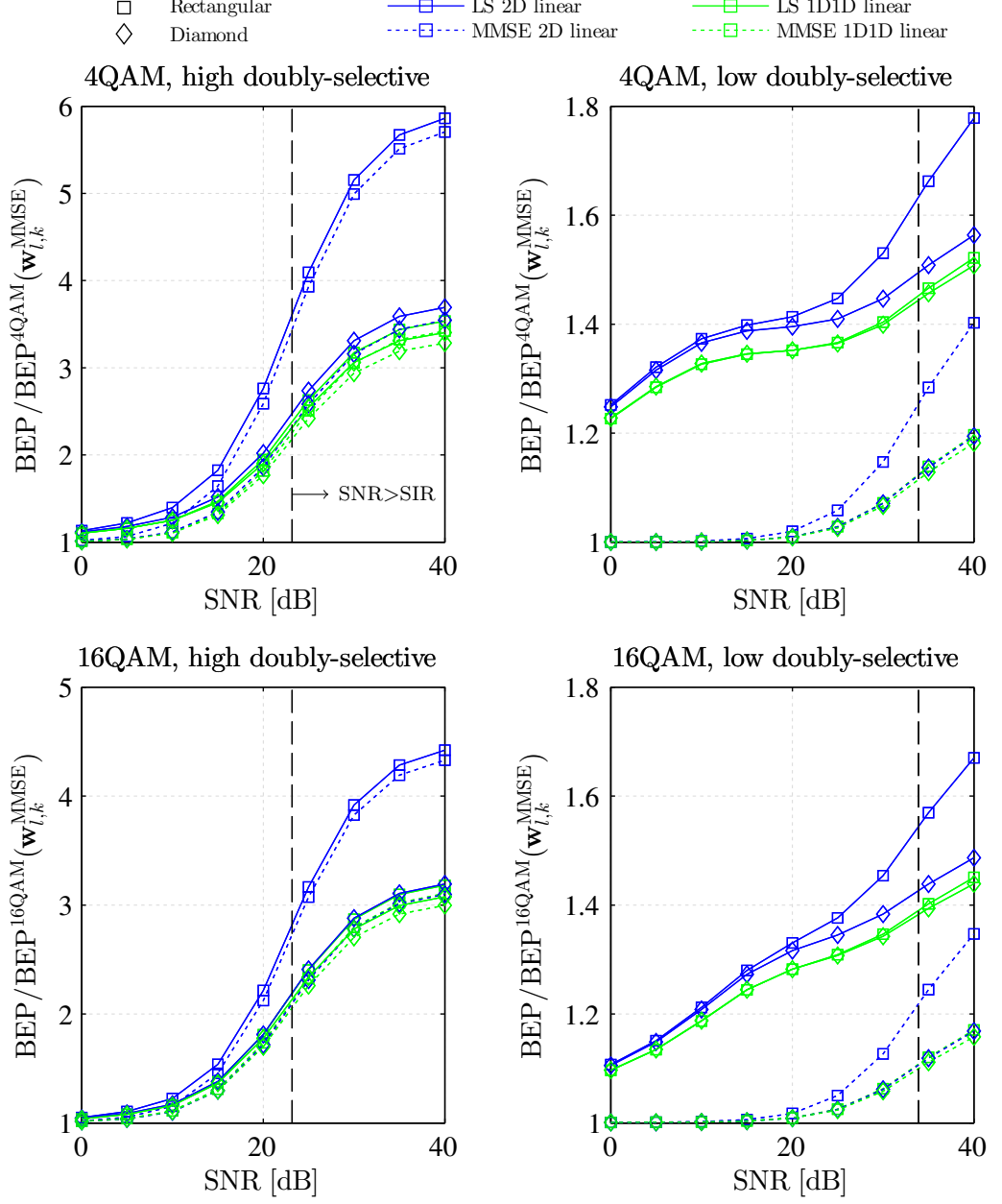


Figure 4.10: Linear Interpolation: successive 1D-1D vs. triangle based 2D, relative BEP as a function of SNR, LS- vs. MMSE-smoother, rectangular-shape vs. diamond-shaped pilot pattern

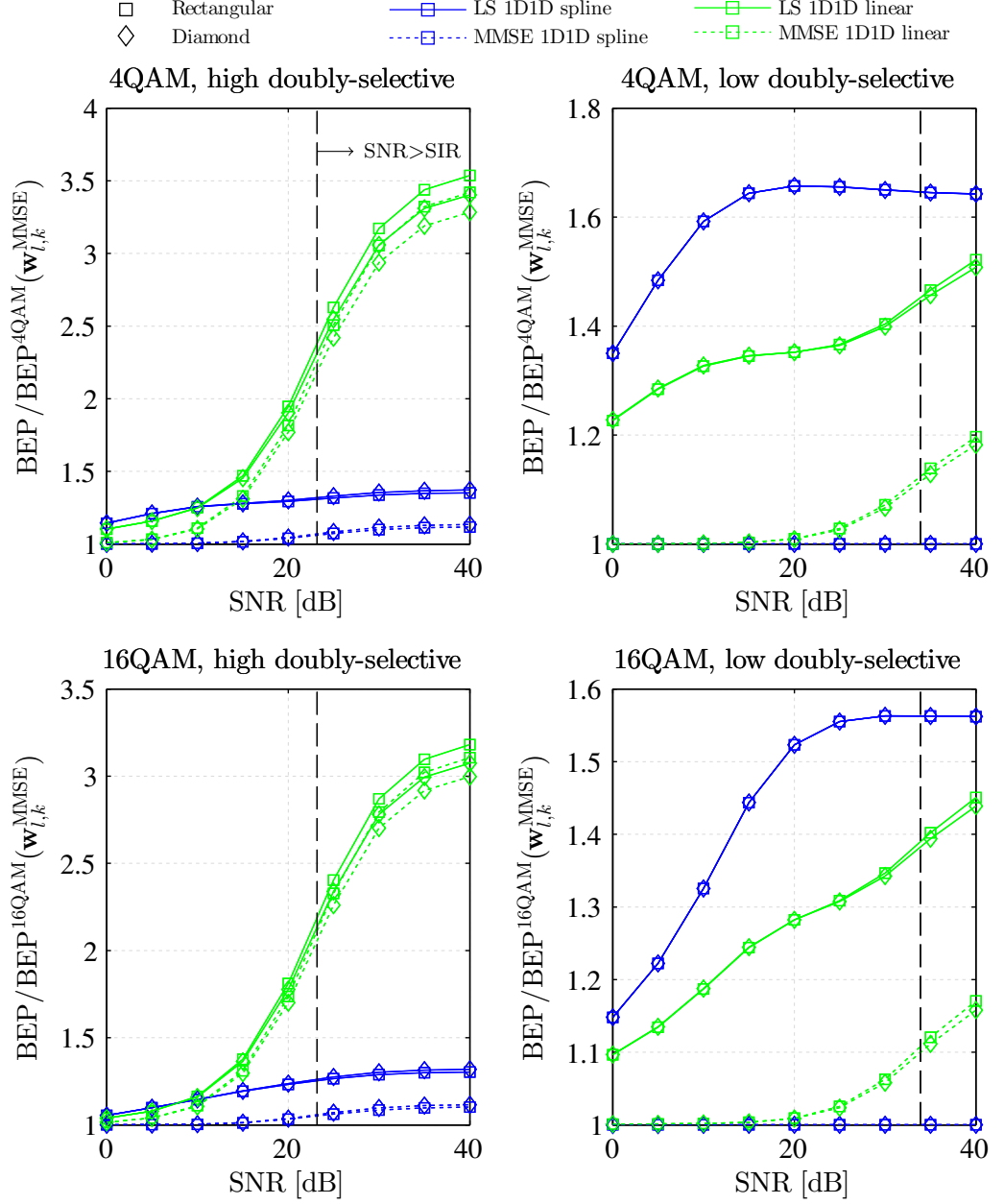


Figure 4.11: Spline Interpolation: relative BEP as a function of SNR, successive 1D-1D as reference, LS- vs. MMSE-smoother, rectangular-shape vs. diamond-shaped pilot pattern

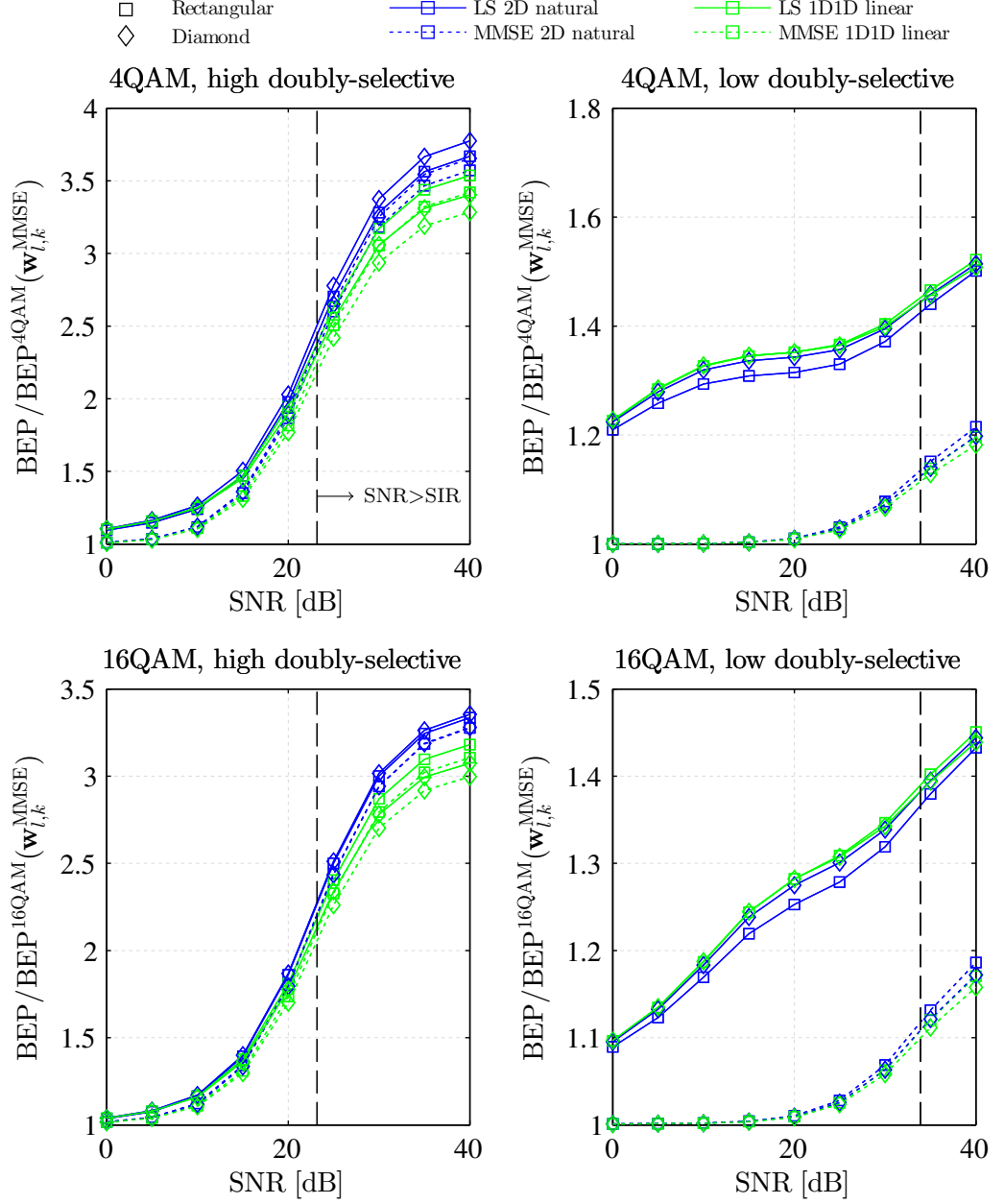


Figure 4.12: Natural Neighbor Interpolation: relative BEP as a function of SNR, successive 1D-1D as reference, LS- vs. MMSE-smoother, rectangular-shape vs. diamond-shaped pilot pattern

## 5. Measurements

In Chapter 4, I derived the BEP for arbitrary interpolation methods whereby simulations confirmed the analytical results. However, simulations are useful but represent only a simplified abstraction and in the end, only the performance in real world scenarios matters. I thus utilize the Vienna Wireless Testbed in order to compare the theoretical BEP to the measured BER.

### 5.1. Overview of the Measurement Set-Up

The Vienna Wireless Testbed performs quasi real-time measurements [27], i.e., the signal is generated off-line, transmitted over a wireless channel in real-time and then again evaluated off-line. For the comparison, I utilize one transmit and two receive antennas<sup>1</sup> out of a total number of four RX and four TX antennas, supported by the testbed. The main parts of the transmitter TX [28] are:

- Digital-to-Analog Converter (DAC): The 16-bit Innovative Integration X5-TX DAC is connected to a personal computer and operates at a sampling frequency  $f_s$  of 200 MHz
- Radio Frequency (RF) front end: It upconverts the signal to 2.5 GHz and consists of an upconverter, a step attenuator, a 20 MHz bandpass filter, and

---

<sup>1</sup> using two RX antennas delivers two measurements at the same time, the system remains single-input and single-output

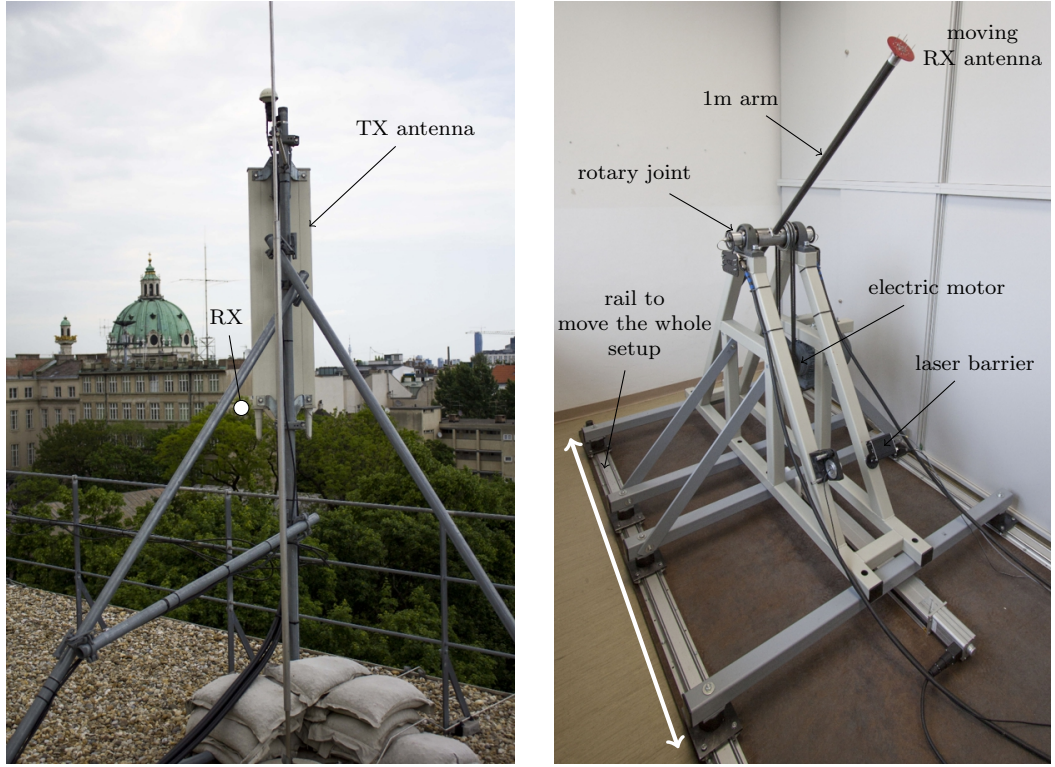


Figure 5.1: Transmit antenna (on the rooftop) and Rotation Unit (indoor, on the 5-th floor)

a power amplifier. The front end is designed for an intermediate frequency  $f_{IF}$  of 70 MHz so that, prior the measurement, the transmit signal has to be digitally upconverted.

- Antenna: The Kathrein Scala Division 60° XX-pol panel antenna (800 10543) is located on the rooftop of our university, as shown in Figure 5.1.

The receiver RX [29] consists of similar elements:

- moving Antenna: The custom build antenna is mounted on a Rotation Unit (see Figure 5.1) and rotates around a central pivot which allows repeatable and controllable measurements at high velocities of up to 560 km/h [30]. The Rotation Unit consists of an electric motor, two rotary joints which connect the rotating cables to the static ones outside the arm, and a laser barrier which is required to determine the position of the antenna. In order to increase the number of independent measurement realizations, the whole setup is placed on a rail so that it can be moved within a range of 0.82 m.
- RF front end: It downconverts the 2.5 GHz signal to 70 MHz and consists of several filters and a low-noise amplifier.

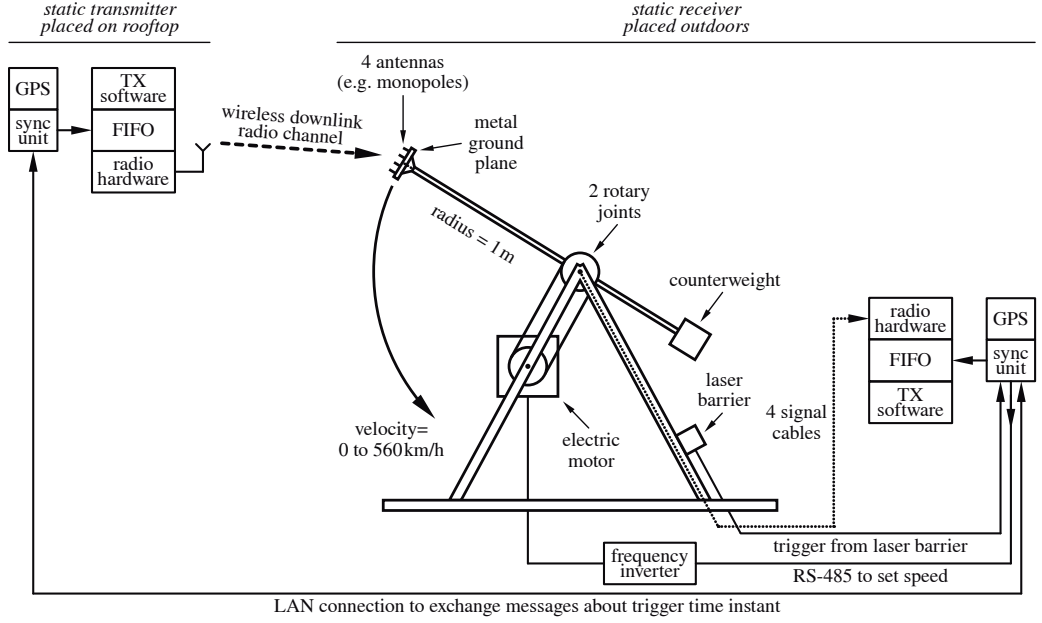


Figure 5.2: Testbed set-up for measuring at high velocities [30]. Note that only two antennas can be used simultaneously (limited by the rotary joint)

- Analog-to-Digital Converter (ADC): The 16-bit Innovative Integration X5-RX ADC is connected to a personal computer and operates also at 200 MHz. Additionally, transmitter and receiver are connected to their own Sync Units [31] which use a Global Positioning System (GPS) module to derive a common time base. Figure 5.2 shows the whole measurement setup. When the antenna passes the laser barrier, a trigger is sent to the Sync Unit, which in turn sends a User Datagram Protocol (UDP) packet over the dedicated Local Area Network (LAN), containing the starting time instance of the transmission. Because the velocity is known, the exact measurement position of the antenna can be determined by a specific delay. In a synchronous way, the TX then starts to transmit the pre-generated signal while at the same time, the RX saves the received samples on a hard drive.

## 5.2. Measurement Methodology

As explained in Section 5.1, the testbed operates at a sampling frequency of 200 MHz and the signal has to be digitally up-converted. OFDM provides an easy method of performing this task in the frequency domain, by rearranging the data symbols  $x_{l,k}$  and appropriate zero padding. I define a new signal vector  $\mathbf{s}_k$  that contains the transmit signal samples for  $kT_s \leq t \leq kT_s + T_s$ , as

described in Section 2.2. The transmit signal vector  $\mathbf{s}_k$  can then be calculated by:

$$\mathbf{s}_k = \text{IFFT} \left\{ \begin{bmatrix} \mathbf{0}_{1 \times \left\lceil \frac{f_{\text{IF}}}{\Delta f} - \frac{L}{2} \right\rceil} & x_{1,k} & \cdots & x_{L,k} & \mathbf{0}_{1 \times \left\lfloor \frac{f_s - 2f_{\text{IF}}}{\Delta f} - L \right\rfloor} & x_{L,k}^* & \cdots & x_{1,k}^* & \mathbf{0}_{1 \times \left\lfloor \frac{f_{\text{IF}}}{\Delta f} - \frac{L}{2} \right\rfloor} \end{bmatrix} \right\}, \quad (5.1)$$

and delivers immediately the proper sampled, up-converted OFDM signal in the time domain. Then, for the cyclic prefix, the last  $\lfloor f_s T_{cp} \rfloor$  samples have to be copied and placed in front. The last step consists of up-scaling the signal and storing it as 16-bit integer on a hard disc. This signal can then be transmitted over a real wireless channel by utilizing the Testbed.

The received data symbols  $y_{l,k}$  can be obtained similar to the signal generation, but in reverse order, i.e., removing the cyclic prefix, FFT, and then choosing the appropriate elements in the frequency domain. Thus, the whole measurement setup can be viewed as a black box where  $x_{l,k}$  represents the input and  $y_{l,k}$  its output. However, one must always keep in mind the limitations imposed by real world hardware and in particular the saturation of the power amplifiers.

The measurement realization  $\{i, a\}$  corresponds to position  $i$ , composed of rail position and angle positions, and to the attenuation<sup>2</sup> index  $a$ . For each realization,  $K + 2$  OFDM symbols are sent over the wireless channel whereas each OFDM symbol consists of  $L + 2$  subcarriers. The time-frequency structure of such a transmission can be written by the transmit symbol matrix  $\check{\mathbf{X}}$  as:

$$\check{\mathbf{X}}^{\{i,a\}} = \begin{bmatrix} 0 & 0 & \cdots & 0 & 0 \\ 0 & x_{1,1}^{\{i,a\}} & \cdots & x_{1,K}^{\{i,a\}} & 0 \\ \vdots & \vdots & \ddots & \vdots & \vdots \\ 0 & x_{L,1}^{\{i,a\}} & \cdots & x_{L,K}^{\{i,a\}} & 0 \\ 0 & 0 & \cdots & 0 & 0 \end{bmatrix}, \quad (5.2)$$

whereas the received symbol matrix  $\check{\mathbf{Y}}^{\{i,a\}}$  exhibits the same structure as  $\check{\mathbf{X}}^{\{i,a\}}$ . The measured BER, as a function of SNR, can then be obtained by averaging the bit error of  $y_{l,k}^{\{i,a\}}$  over all subcarriers, OFDM symbols, and positions.

---

<sup>2</sup> attenuation of the TX-RF front end

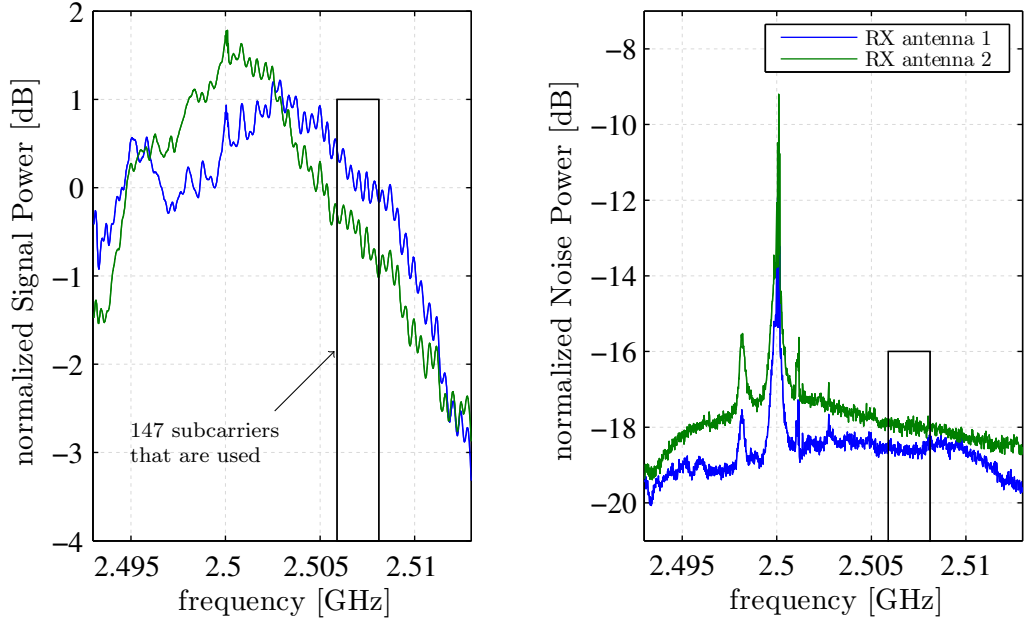


Figure 5.3: Signal Power and Noise Power as a function of the frequency, over 20 MHz, influence of RX antenna

The theoretical BEP, on the other hand, requires the second order channel statistics, which have to be estimated.

The first and last column of  $\check{\mathbf{Y}}^{\{i,a\}}$  can be used to estimate the noise power, while the first and last row give an estimation of the ICI-plus-noise power. Measurements have shown that the main source of ICI is caused by saturation of the power amplifier. I thus reduce the signal power level so that no ICI occurs and calculate the estimated noise power by averaging over all edge-symbols.

Because the absolute value of the received symbols do not matter, I normalize them to have a mean signal power of one. Note that this also implies that the noise power, which was previously constant for different attenuation levels, now depends on  $a$ . The signal power can be calculated as:

$$\hat{P}_{S_{l,k}}^{\{a\}} = \frac{1}{I} \sum_{i=1}^I \left| y_{l,k}^{\{i,a\}} \right|^2 - \hat{P}_{\text{noise}}^{\{a\}}, \quad (5.3)$$

whereas, due to normalization, the time-frequency average of this power has to be one.

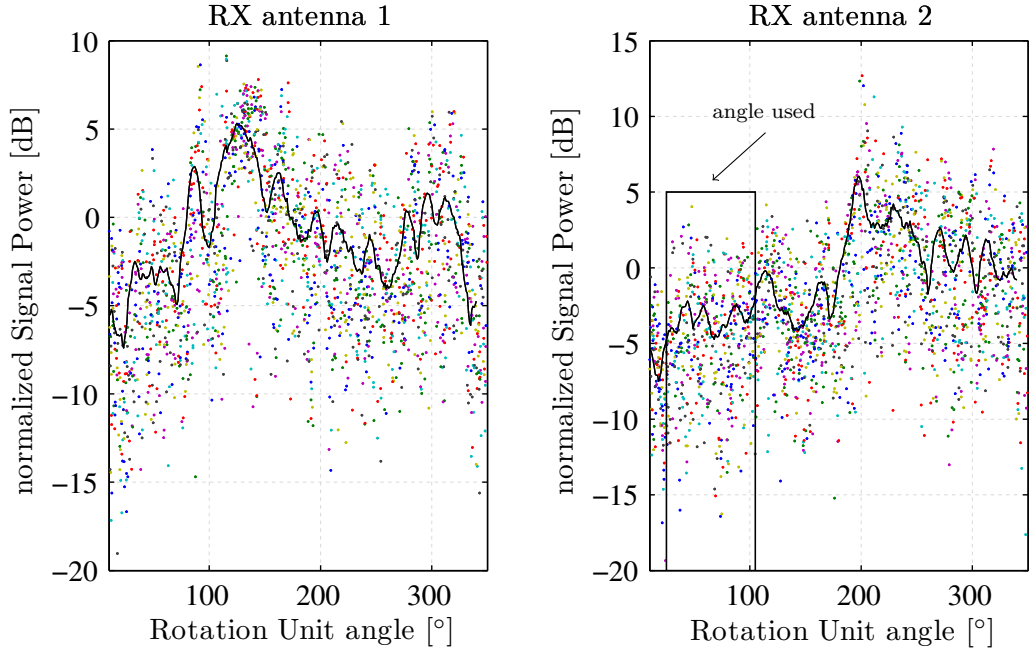


Figure 5.4: Signal Power over Rotation Unit angle

Figure 5.3 shows the signal power<sup>3</sup>  $\hat{P}_{S_{l,k}}^{\{0\}}$  and the noise power  $\hat{P}_{\text{noise}}^{\{0\}}$  as a function of the frequency (subcarrier). At 2.5 GHz, a strong interferer can be identified. I therefore shift the signal to a higher frequency so that the signal- and noise power are relatively constant over the useful bandwidth. This leads to a new intermediate frequency of  $f_{\text{IF}} = 74$  MHz.

Figure 5.4 shows the signal power, averaged over  $l$  and  $k$ , as a function of the angle position<sup>4</sup> whereas each color represents a specific rail position. The black line illustrates the same power, but averaged over 10-degree. The analytical BEP was derived under the condition that the channel coefficients are Gaussian distributed. For that, as a necessary condition, the average signal power has to be constant. According to Figure 5.4, the average normalized power ranges from -5 dB to 5 dB which clearly violates this condition. The physical reason for such a behavior lies in different antenna-polarization, caused by the rotation around a central pivot. I thus use only an angle between 25° and 105°, where the average power is approximately constant.

<sup>3</sup> averaged over  $k$  for the lowest attenuation  $a=0$

<sup>4</sup> the laser barrier is the reference point

Modulation order	4-QAM
Number of subcarriers	145
Number of OFDM symbols	49
Pilot pattern	rectangular
frequency pilot spacing	6
time pilot spacing	4
Carrier frequency	2.507 GHz
Subcarrier spacing	15 kHz
CP duration	4.67 $\mu$ s
Velocity	50 km/h
Angle position range	25° ... 105°
Rail position range	0 ... 0.82 m
Number of random positions	464
Number of attenuation levels	9, in five dB steps

Table 5.1.: Measurement parameters in order to compare the measured BER with the theoretical BEP

The LS channel estimates are given by:

$$\hat{h}_{l,k}^{\text{LS},\{i,a\}} = \frac{y_{l,k}^{\{i,a\}}}{x_{l,k}^{\{i,a\}}}, \quad (5.4)$$

so that the required correlation matrices can be estimated as:

$$\hat{\mathbf{R}}_{\mathbf{h}_{\mathcal{P}}} = \frac{1}{I} \sum_{i=1}^I \hat{\mathbf{h}}_{\mathcal{P}}^{\text{LS},\{i,0\}} \left( \hat{\mathbf{h}}_{\mathcal{P}}^{\text{LS},\{i,0\}} \right)^H - \hat{P}_{\text{noise}}^{\{0\}} \text{diag}(\mathbf{1}_{|\mathcal{P}| \times 1}) \quad (5.5)$$

$$\hat{\mathbf{R}}_{h_{l,k}, \mathbf{h}_{\mathcal{P}}} = \frac{1}{I} \sum_{i=1}^I \hat{\mathbf{h}}^{\text{LS},\{i,0\}} \left( \hat{\mathbf{h}}_{\mathcal{P}}^{\text{LS},\{i,0\}} \right)^H, \quad (5.6)$$

whereas Equation (5.6) is valid only at data positions.

Equation (5.5), (5.6) and (5.3) can then be used to calculate the theoretical BEP for 4-QAM (Equation (4.26)) respectively 16-QAM (Equation (4.42)).

### 5.3. Results

Table 5.1 summarizes the measurement parameters while Figure 5.5 shows the measured BER and the theoretical BEP as a function of the SNR. Both curves coincide quite well whereas any deviation is within the 95% confidence inter-

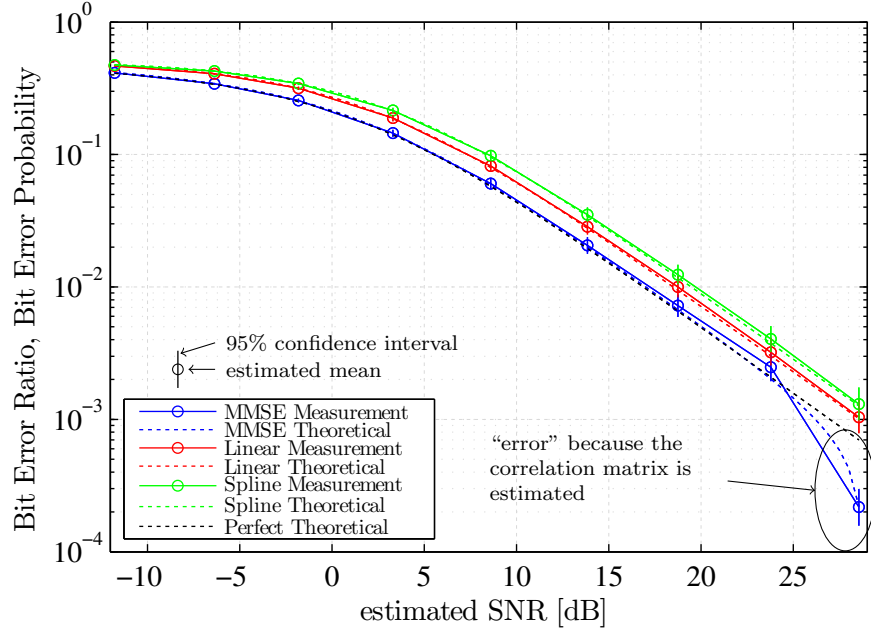


Figure 5.5: measured BER vs. estimated BEP as a function of SNR, influence of different interpolation methods, 4-QAM, 50 km/h, measurements and theory coincide

val<sup>5</sup>. However, for the highest SNR a severe “error<sup>6</sup>” can be identified, because the estimates of the correlation matrices are corrupted by noise. The MMSE estimation then treats the noise as part of the channel, so that the equalizer compensates also a fraction of the noise. Note that the Inequality (4.33) is violated for high SNR, implying a MSE smaller than zero. Nonetheless, further investigation is necessary in order to obtain a more detailed description of this behavior.

Similar to Figure 4.8, the MMSE interpolation performs almost equal to perfect channel knowledge. On the other hand, the BEP for linear interpolation is 20% to 40% higher than the MMSE solution, while for spline interpolation it ranges from 40% to 70%, similar to Figure 4.11. Indeed, the measured channel can be interpreted as “low doubly-selective”, as shown in Figure 5.6. For the calculation of the correlation functions, the LS channel estimates are equalized to have a mean power of one, and a WSSUS channel is assumed. By comparing the autocorrelation functions to the case of a uniform power delay profile and a Jakes Doppler spectrum, a rough approximation of the

<sup>5</sup> obtained by bootstrapping

<sup>6</sup> it actually gives a better BER

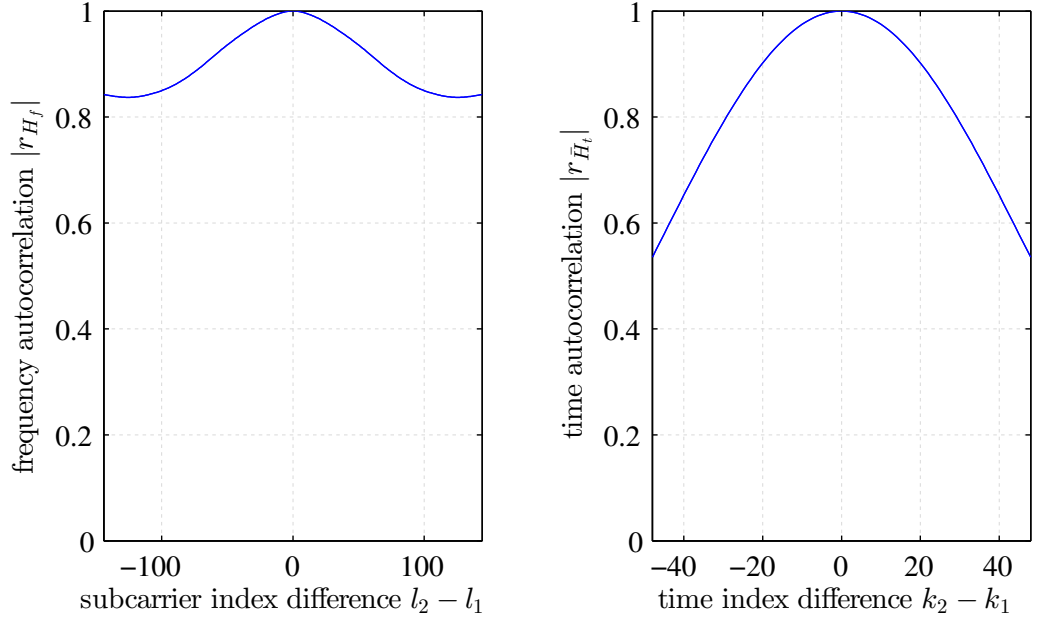


Figure 5.6: Frequency and time autocorrelation

maximum delay and maximum Doppler shift can be found as  $\tau_{\max}\Delta f = 0.0025$  and  $\nu_{\max}T_s = 0.0045$ . Note however, that the measured frequency correlation function severely differentiate from an autocorrelation function obtained by a uniform power delay profile<sup>7</sup>.

<sup>7</sup> corresponds to a sinc-shaped frequency autocorrelation function

## 6. Conclusion and Outlook

In this master thesis, I derived a closed-form expression for the BEP of an LS channel estimator utilizing arbitrary two-dimensional linear interpolation. For 4-QAM, the MMSE interpolation also minimizes the BEP, while for 16-QAM this is accomplished by a scaled MMSE interpolation. However, the potential improvement compared to the unscaled MMSE interpolation is so low, that the scaling factor can be neglected. I separated the channel estimation in a smoothing-part and an interpolation-part. Under the condition of a WSSUS channel, a rectangular-shaped pilot-symbol pattern, and a separable time-frequency correlation function, the optimal two-dimensional interpolation of the MMSE pilot-symbol estimates, can be performed equivalently by successively applying two independent one-dimensional interpolations. For the investigated channel model, one-dimensional linear interpolation first in one direction, and then again in the other direction, slightly outperforms triangular based two-dimensional linear interpolation and, in most cases, natural neighbor interpolation. Spline interpolation, on the other hand, performs completely different. It requires either an MMSE smoother, or a “highly doubly-selective” channel to perform better than linear interpolation. In LTE, the pilot-symbols are so dense together, that diamond-shaped pilot pattern and rectangular-shaped pilot pattern exhibits almost the same performance for practically relevant SINR ranges.

It was shown that the ICI is not Gaussian distributed, so that the closed-form expression of the BEP represents only a close approximation of the true BEP, if the ICI power is larger than the noise power.

Real world measurements, performed with the Vienna Wireless Testbed, confirm the analytical calculations.

For future works, the closed-form expression of the BEP could be straightforwardly extended to higher modulation orders. Additionally, the influence of different interpolation methods for other channel models, like ITU VehA, PedA, or PedB, could be investigated. Finally, more real world measurements for 16-QAM, different velocities, or other TX and RX locations, would strengthen the theoretical results.

## A. OFDM Matrix of a vectorized Channel

By an abuse of notation,  $\mathbf{W}$  can be written as:

$$\mathbf{W} = \frac{1}{N} \exp \left( -j \frac{2\pi}{N} \left( \mathbf{I}_L \otimes \begin{bmatrix} 1 \\ \vdots \\ L \end{bmatrix} - \begin{bmatrix} 1 & 0 & 0 \\ 0 & \ddots & 0 \\ 0 & 0 & L \end{bmatrix} \otimes \mathbf{1}_{L \times 1} \right) \otimes \begin{bmatrix} 0 & \cdots & N-1 \end{bmatrix} \right) \circ (\mathbf{I}_L \otimes \mathbf{1}_{L \times N}). \quad (\text{A.1})$$

Here,  $\exp(\cdot)$  denotes the exponential function, applied on each element in the matrix. The Kronecker product  $\mathbf{I}_L \otimes \mathbf{1}_{L \times N}$  together with the Hadamard product  $\circ$  (entry-wise multiplication) is needed to set the non-diagonal blocks to zero.

## B. Correlation Matrices for a 2D separable WSSUS Channel

For the derivation of the correlation matrices I make the following assumptions:

- WSSUS channel
- separable time-frequency correlation

The time correlation matrix for OFDM symbol time  $k_1$  and  $k_2$ , can then be found as:

$$\mathbf{R}_{H_t}[k_1-k_2] = r_{H_t} \left( \left( \left( \begin{bmatrix} 0 & -1 & \cdots & -(N-1) \\ 1 & 0 & \ddots & : \\ : & \ddots & \ddots & : \\ (N-1) & \cdots & \cdots & 0 \end{bmatrix} + (k_1 - k_2)(N + N_{cp}) \right) \Delta t \right) \right). \quad (\text{B.1})$$

The time correlation function  $r_{H_t}(\cdot)$  (see Section 2.1) is applied on each element of the matrix and the variable  $\Delta t = T_s/N$  represents the sampling time. In a similar way the frequency correlation matrix becomes:

$$\mathbf{R}_{H_f} = r_{H_f} \left( \left( \begin{bmatrix} 0 & -1 & \cdots & -(L-1) \\ 1 & 0 & \ddots & : \\ : & \ddots & \ddots & : \\ (L-1) & \cdots & \cdots & 0 \end{bmatrix} \Delta f \right) \right), \quad (\text{B.2})$$

so that the correlation matrix of the vectorized transfer-function matrix can be written as:

$$\mathbf{R}_{\text{vec}\{\mathbf{H}_k\}} = \mathbf{R}_{H_t}[0] \otimes \mathbf{R}_{H_f}, \quad (\text{B.3})$$

The correlation between elements of the OFDM matrix  $\mathbf{D}_k$  (see Equation (2.25)) can be found as:

$$\begin{aligned} \mathbb{E} \left\{ (\mathbf{D}_{k_1})_{l_1, d_1} (\mathbf{D}_{k_2})_{l_2, d_2}^* \right\} &= \exp \left( -j \frac{2\pi(l_1 - d_1)}{N} \begin{bmatrix} 0 & \dots & N-1 \end{bmatrix} \right) \mathbf{R}_{H_t}[k_1 - k_2] \\ &\quad (\mathbf{R}_{H_f})_{d_1, d_2} \exp \left( +j \frac{2\pi(l_2 - d_2)}{N} \begin{bmatrix} 0 \\ \dots \\ N-1 \end{bmatrix} \right) \end{aligned} \quad (\text{B.4})$$

For the calculation of the BEP, only the diagonal elements of  $\mathbf{D}_k$  are of interests i.e. the piecewise time average of the channel. The correlation function of theses piecewise time averages  $r_{\bar{H}_t}$  can be calculated by using Equation (B.4) and setting  $l_1 = d_1$  and  $l_2 = d_2$ , so that:

$$r_{\bar{H}_t}[k_1 - k_2] = \frac{1}{N^2} \begin{bmatrix} 0 & \dots & N-1 \end{bmatrix} \mathbf{R}_{H_t}[k_1 - k_2] \begin{bmatrix} 0 \\ \dots \\ N-1 \end{bmatrix} \quad (\text{B.5})$$

I now define a pilot index vector  $\mathbf{i}_{p_r}$  that gives the row index of the pilot symbols in a vectorized form<sup>1</sup>. Similar, the index vector  $\mathbf{i}_{p_c}$  gives the column index. For example a pilot structure as given in Figure 4.1 leads to:  $\mathbf{i}_{p_r} = \begin{bmatrix} 1 & 6 & 14 & 9 & 8 & 12 & 4 & 13 & 3 & 8 \end{bmatrix}^T$  and  $\mathbf{i}_{p_c} = \begin{bmatrix} 0 & 1 & 1 & 2 & 4 & 5 & 6 & 7 & 9 & 10 \end{bmatrix}^T$ . Using these pilot index vectors, the correlation matrix  $\mathbf{R}_{\mathbf{h}_p}$  can be found as:

$$\mathbf{R}_{\mathbf{h}_p} = r_{H_f} \left( (\mathbf{i}_{p_r} \mathbf{1}_{1 \times |\mathcal{P}|} - (\mathbf{i}_{p_r} \mathbf{1}_{1 \times |\mathcal{P}|})^T) \Delta f \right) \circ r_{\bar{H}_t} [\mathbf{i}_{p_c} \mathbf{1}_{1 \times |\mathcal{P}|} - (\mathbf{i}_{p_c} \mathbf{1}_{1 \times |\mathcal{P}|})^T], \quad (\text{B.6})$$

where the correlation functions  $r_{H_f}(\cdot)$  and  $r_{\bar{H}_t}[\cdot]$  are again applied for each matrix element.

<sup>1</sup> in Matlab  $[\mathbf{i}_{p_r}, \mathbf{i}_{p_c}] = \text{find}(\text{pilotmatrix})$  can be used, whereas the pilotmatrix is a  $L \times K$  matrix that consists of zeros at data position and ones at pilot position

Similar to the pilot index vectors, I define all index vectors  $\mathbf{i}_{a_r}$  and  $\mathbf{i}_{a_c}$ , which give the index of every symbol in a vectorized form. The correlation matrix  $\mathbf{R}_{\mathbf{h}, \mathbf{h}_{\mathcal{P}}}$  can then be obtained as:

$$\mathbf{R}_{\mathbf{h}, \mathbf{h}_{\mathcal{P}}} = r_{H_f} \left( (\mathbf{i}_{a_r} \mathbf{1}_{1 \times |\mathcal{P}|} - (\mathbf{i}_{p_r} \mathbf{1}_{1 \times LK})^T) \Delta f \right) \circ r_{\bar{H}_t} [\mathbf{i}_{a_c} \mathbf{1}_{1 \times |\mathcal{P}|} - (\mathbf{i}_{p_c} \mathbf{1}_{1 \times LK})^T] \quad (\text{B.7})$$

Another way of calculating the correlation matrices  $\mathbf{R}_{\mathbf{h}_{\mathcal{P}}}$  and  $\mathbf{R}_{\mathbf{h}, \mathbf{h}_{\mathcal{P}}}$  can be found by taking the right elements<sup>2</sup> of the large correlation matrix

$$\mathbf{R}_{\mathbf{h}} = \mathbf{R}_{\bar{H}_t} \otimes \mathbf{R}_{H_f}. \quad (\text{B.8})$$

However, Equation (B.6) and (B.7) have the advantage that they can be easily extended to the case of non-WSSUS and non-separability.

## C. BEP for 16-QAM

The BEP for 16-QAM was derived in Section 4.2.2, but due to the length of the equations, the closed-form expressions were omitted. Equation (C.1) gives a general formula for the second and forth bit, while Equation (C.2) gives the BEP under the assumption that  $\Re\{\mathbf{R}_{h_{l,k}, \hat{\mathbf{h}}_{\mathcal{P}}^{\text{LS}}} \mathbf{w}_{l,k}\} > 0$  and  $\Im\{\mathbf{R}_{h_{l,k}, \hat{\mathbf{h}}_{\mathcal{P}}^{\text{LS}}} \mathbf{w}_{l,k}\} = 0$ .

Equation (C.3) delivers a closed-form expression for the conditional probability that the real part of  $\hat{x}_{l,k}$  is smaller than a given constant.

---

<sup>2</sup> in Matlab  $\mathbf{R}_{\mathbf{h}_{\mathcal{P}}} = \mathbf{R}_{\mathbf{h}}(\text{pilotmatrix}(:), \text{pilotmatrix}(:))$  and  $\mathbf{R}_{\mathbf{h}, \mathbf{h}_{\mathcal{P}}} = \mathbf{R}_{\mathbf{h}}(:, \text{pilotmatrix}(:))$

$$\begin{aligned} \text{BEP}_{l,k}^{16\text{QAM, Bit2\&4}}(\mathbf{w}_{l,k}) = & \frac{1}{2} - \frac{1}{16} \sum_{\substack{q_r \in \{-3, \\ \{1,3\}\}}} \sum_{\substack{q_i \in \{-3, \\ \{-1,1,3\}\}}} \frac{q_r \Re\{\mathbf{R}_{h_{l,k}, \hat{\mathbf{h}}_P^{\text{LS}} \mathbf{w}_{l,k}}\} - q_i \Im\{\mathbf{R}_{h_{l,k}, \hat{\mathbf{h}}_P^{\text{LS}} \mathbf{w}_{l,k}}\}}{\sqrt{[(q_r^2 + q_i^2)P_{S_{l,k}} + 10(P_{\text{ICI}_{l,k}} + P_{\text{noise}_{l,k}})] \mathbf{w}_{l,k}^H \mathbf{R}_{\hat{\mathbf{h}}_P^{\text{LS}} \mathbf{w}_{l,k}} - (q_i \Re\{\mathbf{R}_{h_{l,k}, \hat{\mathbf{h}}_P^{\text{LS}} \mathbf{w}_{l,k}}\} + q_r \Im\{\mathbf{R}_{h_{l,k}, \hat{\mathbf{h}}_P^{\text{LS}} \mathbf{w}_{l,k}}\})^2}} \end{aligned} \quad (\text{C.1})$$

$$\widetilde{\text{BEP}}_{l,k}^{16\text{QAM, Bit2\&4}}(\mathbf{w}_{l,k}) = \frac{1}{2} - \frac{1}{8} \sum_{\substack{q_r \in \{1,3\}}} \sum_{\substack{q_i \in \{1,3\}}} \frac{1}{\sqrt{[(q_r^2 + q_i^2)P_{S_{l,k}} + 10(P_{\text{ICI}_{l,k}} + P_{\text{noise}_{l,k}})] \frac{\mathbf{w}_{l,k}^H \mathbf{R}_{\hat{\mathbf{h}}_P^{\text{LS}} \mathbf{w}_{l,k}}}{q_r^2} - \frac{q_i^2}{q_r^2}}}}, \quad (\text{C.2})$$

$$\begin{aligned} \Pr\left(\Re\left\{\frac{y_{l,k}}{\hat{h}_{l,k}}\right\} < \frac{a}{\sqrt{10}} \left| \frac{q_r + \mathbf{j}q_i}{\sqrt{10}} \right| = \frac{1}{2} - \frac{1}{2}\right) = & \frac{q_r \Re\{\mathbf{R}_{h_{l,k}, \hat{\mathbf{h}}_P^{\text{LS}} \mathbf{w}_{l,k}}\} - q_i \Im\{\mathbf{R}_{h_{l,k}, \hat{\mathbf{h}}_P^{\text{LS}} \mathbf{w}_{l,k}}\} - a \mathbf{w}_{l,k}^H \mathbf{R}_{\hat{\mathbf{h}}_P^{\text{LS}} \mathbf{w}_{l,k}}}{\sqrt{[(q_r^2 + q_i^2)P_{S_{l,k}} + 10(P_{\text{ICI}_{l,k}} + P_{\text{noise}_{l,k}})] - 2a \left( q_r \Re\{\mathbf{R}_{h_{l,k}, \hat{\mathbf{h}}_P^{\text{LS}} \mathbf{w}_{l,k}}\} - q_i \Im\{\mathbf{R}_{h_{l,k}, \hat{\mathbf{h}}_P^{\text{LS}} \mathbf{w}_{l,k}}\} + a^2 \mathbf{w}_{l,k}^H \mathbf{R}_{\hat{\mathbf{h}}_P^{\text{LS}} \mathbf{w}_{l,k}} \right) - (q_i \Re\{\mathbf{R}_{h_{l,k}, \hat{\mathbf{h}}_P^{\text{LS}} \mathbf{w}_{l,k}}\} + q_r \Im\{\mathbf{R}_{h_{l,k}, \hat{\mathbf{h}}_P^{\text{LS}} \mathbf{w}_{l,k}}\})^2}} \end{aligned} \quad (\text{C.3})$$

---

# Acronyms

<b>1D</b>	one-Dimensional
<b>2D</b>	two-Dimensional
<b>ADC</b>	Analog-to-Digital Converter
<b>BEP</b>	Bit Error Probability
<b>BER</b>	Bit Error Ratio
<b>DAC</b>	Digital-to-Analog Converter
<b>DVB-T</b>	Digital Video Broadcasting - Terrestrial
<b>FFT</b>	Fast Fourier Transform
<b>GPS</b>	Global Positioning System
<b>ICI</b>	Inter-Carrier Interference
<b>IFFT</b>	Inverse Fast Fourier Transform
<b>ISI</b>	Inter Symbol Interference
<b>LAN</b>	Local Area Network
<b>LS</b>	Least Squares
<b>LTE</b>	Long Term Evolution
<b>LTV</b>	Linear Time Variant
<b>MMSE</b>	Minimum Mean Squared Error
<b>MSE</b>	Mean Squared Error
<b>OFDM</b>	Orthogonal Frequency Division Multiplexing
<b>PACE</b>	Pilot-symbol-Aided Channel Estimation

---

**pdf** probability density function  
**QAM** Quadrature Amplitude Modulation  
**RF** Radio Frequency  
**SINR** Signal-to-Interference-plus-Noise Ratio  
**SIR** Signal-to-Interference Ratio  
**SNR** Signal-to-Noise Ratio  
**UDP** User Datagram Protocol  
**WLAN** Wireless Local Area Network  
**WSSUS** Wide-Sense Stationary Uncorrelated Scattering

# Bibliography

- [1] R. W. Chang, "Synthesis of Band-Limited Orthogonal Signals for Multichannel Data Transmission," *Bell Systems Technical Journal*, vol. 45, pp. 1775–1796, Dec. 1966.
- [2] P. Robertson and S. Kaiser, "The effects of doppler spreads in OFDM(A) mobile radio systems," in *Vehicular Technology Conference, 1999. VTC 1999 - Fall. IEEE VTS 50th*, vol. 1, 1999, pp. 329–333 vol.1.
- [3] M. Russell and G. Stuber, "Interchannel interference analysis of OFDM in a mobile environment," in *Vehicular Technology Conference, 1995 IEEE 45th*, vol. 2, 1995, pp. 820–824 vol.2.
- [4] A. Hutter, R. Hasholzner, and J. Hammerschmidt, "Channel estimation for mobile OFDM systems," in *Vehicular Technology Conference, 1999. VTC 1999 - Fall. IEEE VTS 50th*, vol. 1, 1999, pp. 305–309 vol.1.
- [5] T. C. W. Schenk, R. van Der Hofstad, E. Fledderus, and P. F. M. Smulders, "Distribution of the ICI term in phase noise impaired OFDM systems," *IEEE Transactions on Wireless Communications*, vol. 6, no. 4, pp. 1488–1500, 2007.
- [6] J. Zhang, L.-L. Yang, X. Liu, and L. Hanzo, "Inter-carrier interference analysis of OFDM systems communicating over rapidly-fading nakagami-m channels," in *IEEE Ninth International Symposium on Spread Spectrum Techniques and Applications*, 2006, pp. 79–83.
- [7] X. Dong, W.-S. Lu, and A. Soong, "Linear interpolation in pilot symbol assisted channel estimation for OFDM," *IEEE Transactions on Wireless Communications*, vol. 6, no. 5, pp. 1910–1920, 2007.
- [8] M.-H. Hsieh and C.-H. Wei, "Channel estimation for OFDM systems based on comb-type pilot arrangement in frequency selective fading channels," *IEEE Transactions on Consumer Electronics*, vol. 44, no. 1, pp. 217–225, 1998.
- [9] S. Coleri, M. Ergen, A. Puri, and A. Bahai, "Channel estimation techniques based on pilot arrangement in OFDM systems," *IEEE Trans. Broadcasting*, vol. 48, pp. 223–229, 2002.
- [10] M. Yalcin and A. Akan, "Doubly-selective channel estimation for OFDM systems," in *Communications (MICC), 2009 IEEE 9th Malaysia International Conference on*, 2009, pp. 6–10.
- [11] F. Hlawatsch and G. Matz, *Wireless Communications over Rapidly Time-Varying Channels*. Amsterdam, The Netherlands: Academic Press, 2011.
- [12] A. Molisch, *Wireless Communications*. Wiley, 2005.

- [13] P. Bello, "Characterization of randomly time-variant linear channels," *IEEE Transactions on Communications Systems*, vol. 11, no. 4, pp. 360–393, 1963.
- [14] P. Hoeher, "A statistical discrete-time model for the WSSUS multipath channel," *IEEE Transactions on Vehicular Technology*, vol. 41, no. 4, pp. 461–468, 1992.
- [15] P. Hoeher, S. Kaiser, and P. Robertson, "Pilot-symbol-aided channel estimation in time and frequency," in *In Proc. IEEE Global Telecommunications Conference (GLOBECOM 97), Communication Theory Mini-Conference*, 1997, pp. 90–96.
- [16] Y. G. Li and G. L. Stuber, *Orthogonal Frequency Division Multiplexing for Wireless Communications*. Springer, 2006.
- [17] A. Peled and A. Ruiz, "Frequency domain data transmission using reduced computational complexity algorithms," in *IEEE International Conference on Acoustics, Speech, and Signal Processing*, vol. 5, 1980, pp. 964–967.
- [18] R. G. Gallager, "Circularly-symmetric gaussian random vectors," 2008. [Online]. Available: <http://www.rle.mit.edu/rgallager/documents/CircSymGauss.pdf>
- [19] P. Hoeher, S. Kaiser, and P. Robertson, "Two-dimensional pilot-symbol-aided channel estimation by Wiener filtering," vol. 3, pp. 1845–1848 vol.3, 1997.
- [20] C.-H. Yih, "Effects of channel estimation error in the presence of CFO on OFDM BER in frequency-selective rayleigh fading channels," *JCM*, vol. 3, no. 3, pp. 10–18, 2008.
- [21] T. K. Moon and W. C. Stirling, *Mathematical Methods and Algorithms for Signal Processing*. Prentice Hall, 1999.
- [22] G. Auer and E. Karipidis, "Pilot aided channel estimation for OFDM: a separated approach for smoothing and interpolation," in *IEEE International Conference on Communications*, vol. 4, 2005, pp. 2173–2178 Vol. 4.
- [23] M. Simko, "Pilot pattern optimization for doubly-selective MIMO OFDM transmissions," Ph.D. dissertation, E389, Vienna University of Technology, 2013.
- [24] M. Unser, "Splines: a perfect fit for signal and image processing," *Signal Processing Magazine, IEEE*, vol. 16, no. 6, pp. 22–38, 1999.
- [25] A. Marganitz. (2012) Interpolation. [Online]. Available: <http://public.beuth-hochschule.de/~marganit/Interpolation.pdf>
- [26] R. Sibson, *A Brief Description of Natural Neighbour Interpolation*. John Wiley & Sons, 1981, vol. 21, pp. 21–36.
- [27] S. Caban, "Testbed-based evaluation of mobile communication systems," Ph.D. dissertation, Institut für Nachrichtentechnik und Hochfrequenztechnik, 2009.
- [28] E. Huremovic, "Wireless testbed transmitter," Master's thesis, E389, 2012.
- [29] H. Haderer, "Wireless testbed receiver," Master's thesis, E389, 2012.
- [30] S. Caban, J. Rodas, and J. A. García Naya, "A methodology for repeatable, off-line, closed-loop wireless communication system measurements at very high velocities of up to 560 km/h," in *Proc. 2011 IEEE International Instrumentation and Measurement Technology Conference (I2MTC2011)*, 2011.

- [31] A. Disslbacher-Fink, “Hardware-based timing synchronization,” Master’s thesis, E389, 2011.